ANNUAL REVIEWS

Annual Review of Physical Chemistry

Mechanisms of

Photothermalization in

Plasmonic Nanostructures:

Insights into the Steady State

Shengxiang Wu¹ and Matthew Sheldon²

- ¹Beijing Computational Science Research Center, Beijing, China; email: sxwu@csrc.ac.cn
- ²Department of Chemistry and Department of Materials Science and Engineering, Texas A&M University, College Station, Texas, USA; email: sheldonm@tamu.edu



www.annualreviews.org

- · Download figures
- Navigate cited references
- Keyword search
- · Explore related articles
- Share via email or social media

Annu. Rev. Phys. Chem. 2023. 74:521-45

First published as a Review in Advance on February 15, 2023

The *Annual Review of Physical Chemistry* is online at physchem.annualreviews.org

https://doi.org/10.1146/annurev-physchem-062422-014911

Copyright © 2023 by the author(s). This work is licensed under a Creative Commons Attribution 4.0 International License, which permits unrestricted use, distribution, and reproduction in any medium, provided the original author and source are credited. See credit lines of images or other third-party material in this article for license information.



Keywords

metallic nanoparticle, nonthermal carriers, hot electrons, steady state, Raman thermometry, photocatalysis

Abstract

Localized surface plasmon resonances (LSPRs) in metallic nanostructures result in subwavelength optical confinement that enhances light–matter interactions, for example, aiding the sensitivity of surface spectroscopies. The dissipation of surface plasmons as electronic and vibrational excitations sets the limit for field confinement but also provides opportunities for photochemistry, photocatalysis, and photothermal heating. Optimization for either goal requires a deeper understanding of this photothermalization process. In this review, we focus on recent insights into the physics and dynamics governing photothermalization of LSPRs in metallic nanostructures, emphasizing comparisons between the steady-state behavior and ultrafast time-resolved studies. The differences between these regimes inform how to best optimize plasmonic systems for applications under relatively low-intensity, continuous illumination (e.g., sunlight).

1. INTRODUCTION

Coupling between collective oscillations of electrons and electromagnetic fields at optical frequencies, termed surface plasmons, provides an ideal platform to analyze light-matter interactions across a wide range of the electromagnetic spectrum, from ultraviolet to infrared, depending on the density of free conduction carriers in a material. Common plasmonic materials include coinage metals (e.g., gold, silver, and copper) and aluminum, an earth-abundant material. Thanks to advancements in synthetic and nanofabrication techniques using both wet-lab methods (bottom-up) and lithography (top-down), metallic nanostructures with precise size and geometry can be prepared, making them a widely studied platform in the plasmonics, nanophotonics, and physical chemistry research communities.

As shown in **Figure 1**, this review is structured to discuss topics in an order that mirrors the microscopic timeline that underlies the photophysics of plasmon excitation, relaxation, and energy dissipation into a surrounding environment. We summarize recent theoretical and experimental improvements in our understanding of

- optical field concentration at plasmonic hot spots;
- optical absorption and excitation of large nonthermal, nonequilibrium carrier populations;
- electron-electron scattering of nonthermal carriers, leading to thermalized hot electron subpopulations out of equilibrium with the vibrational temperature of the system;
- coupling between nonequilibrium carriers and phonons that increases vibrational activation;
 and
- heating within and around a nanostructure, and the thermometry techniques being developed to analyze these complex environments.

In addition to enhancing light-matter interactions that can aid sensing and spectroscopy, plasmonic phenomena excite large nonequilibrium carrier populations that can drive optoelectronic processes or photocatalytic chemical reactions, as well as applications that benefit from pronounced local heating.

1.1. Plasmonic Hot Spots and Localized Surface Plasmon Resonances

When a plasmon is geometrically constrained within a nanostructure, electromagnetic fields strongly drive the mechanical resonance of the charge density wave, giving rise to a localized surface plasmon resonance (LSPR). The resonance frequency, ω_{SP} , depends on the metal composition, the surrounding medium, and the geometry of the nanostructure (1, 2). Extreme subwavelength light confinement occurs near corners and edges, and the concentrated optical energy and electric near field (E) is termed the plasmonic hot spot (**Figure 1**a). Not surprisingly, many surface spectroscopies that rely on transitions between electronic or vibronic states have benefited from plasmonic hot spots. A notable example is surface-enhanced Raman spectroscopy (SERS), which has achieved single-molecule sensing (3–5). A major research goal in plasmonics is therefore dedicated to understanding near-field confinement for sensing applications. For instance, even stronger light confinement can be achieved within a subnanometer gap of plasmonic dimers, though the tunneling of electrons back and forth between two plasmonic nanostructures (a so-called charge transfer plasmon) is believed to decrease the magnitude of field confinement (6).

In general, absorption and the consequent photothermalization—the dissipation of absorbed optical energy as heat—set another upper limit for field confinement (7, 8). Indeed, the plasmonics community commonly describes a plasmon resonance and the associated near-field concentration with a quality factor, Q-factor, which is defined as $Q = \omega_{SP}/2\gamma$, where $\gamma = \text{Im}[\varepsilon_m(\omega)]/\partial_\omega \text{Re}[\varepsilon_m(\omega)]$

is the plasmon decay rate, and ε_m is the metal permittivity. The imaginary part of the permittivity, $\text{Im}[\varepsilon_m(\omega)]$, is also closely related to the absorption of optical power, $P_{\text{abs}} = -0.5\omega |E|^2 \text{Im}[\varepsilon_m(\omega)]$. This suggests that optical absorption has a twofold importance: (a) Extreme near-field concentration for advanced sensing applications requires a deep understanding of how absorption and photothermalization occur, and (b) as elaborated throughout this review, optical absorption is followed by a series of microscopic electronic and vibrational excitations that have enabled new strategies for photocatalysis (9–16), photodetection (17, 18), solar energy harvesting (19), photothermal catalysis (20, 21), photoacoustic imaging (22), heat-assisted magnetic recording (23, 24), thermo-photovoltaics (25), and photothermal therapy (26–28), among other applications.

This review focuses primarily on the physical chemistry and the microscopic mechanisms of photothermalization after excitation of the LSPR. The topics we discuss include nonradiative damping (Landau damping) of surface plasmons, electron-electron (e-e) and electron-phonon (e-ph) scattering within a metallic nanostructure, the two-temperature model (TTM) established from ultrafast studies, and a recently developed Raman thermometry method for probing the population of electronic states. Given that continuous-wave (CW) illumination is more closely related to applications for harvesting solar energy, a major focus in the research community, we also discuss and emphasize the differences between photothermalization during time-resolved pump-probe studies and photothermalization during steady-state scenarios.

1.2. The Two-Temperature Model and Comparisons Between Ultrafast Studies and Continuous Wave Studies

Historically, the mechanisms of photothermalization in metallic nanostructures, such as transient absorption, transmission, or reflectivity, have been analyzed by ultrafast time-resolved pumpprobe spectroscopy. The underlying physics are derived from the correspondence between the population of electronic states and the optical behavior of the metal. In a typical ultrafast setup, two optical pulses are used: an intense pump pulse drives the metallic nanostructure out of equilibrium, and after a time delay (approximately tens of femtoseconds to picoseconds), a second optical pulse (the probe) analyzes the perturbed electronic structure at a given spectral position (energy) and time delay. Because the transient signal is due to the perturbed electronic population, the electronic population that remains unchanged during the pump pulse does not contribute to the signal. Further, due to the short interval of the pump pulse, intense optical power is usually used to excite as many electrons as possible out of equilibrium. This ultrafast technique is an excellent tool to study the time evolution of electrons in metals. Alternatively, a CW measurement can provide insight into photothermalization in a steady state. A major difference between the two types of experiments is that the incident optical power used in a CW measurement can be much lower than that used in ultrafast studies. Additionally, the electronic states are continually perturbed by sequential incident photons. These two scenarios, ultrafast and CW, may be bridged by a plasmonic nanostructure, because the optical power absorbed at plasmonic hot spots is highly concentrated and may become comparable to that in an ultrafast study of a bulk metal, even under CW illumination. In fact, this extreme power and field concentration are the origin of many nonlinear effects observed in plasmonic nanostructures (29, 30). Therefore, ultrafast experiments provide a good starting point for researchers to discuss the photothermalization of carriers and to compare with CW experiments.

Here, we briefly describe the TTM (Equation 1) that has been developed from ultrafast studies (31): A metal absorber is divided into two connected subsystems, the electron subsystem and the phonon subsystem. The dynamics of these two subsystems are governed by two differential

equations, one for the evolution of the electron subsystem, which is driven by the absorbed optical energy (Equation 1a), and the other for the evolution of the phonon subsystem, which is excited by e-ph interactions and relaxes through conduction (Equation 1b) (for a detailed discussion, see Section 3). Indeed, the decoupling of these two subsystems is justified by the small electronic heat capacity C_e compared with phononic heat capacity C_l . It is assumed that optical energy is first deposited into the electron subsystem only, and the two subsystems are connected through an e-ph interaction coefficient G. Other parameters in the TTM include the electron temperature T_e and the phonon temperature T_l . The κ_e and κ_l are the electronic thermal conductivity and phononic thermal conductivity, respectively. S represents the laser energy deposition per unit volume and unit time. Strictly speaking, the temperature, heat capacity, and thermal conductivity are spatially dependent; however, this complexity is conventionally neglected, assuming homogeneous photoexcitation and thermalization,

$$\frac{\partial (C_{e}T_{e})}{\partial t} = \nabla(\kappa_{e}\nabla T_{e}) - G(T_{e} - T_{l}) + S(r, t),$$
 1a.

$$\frac{\partial (C_l T_l)}{\partial t} = \nabla (\kappa_l \nabla T_l) + G(T_e - T_l).$$
 1b.

For a nanostructure illuminated at the LSPR with CW or pulsed excitation, the assumption of homogeneous photoexcitation without spatial temperature gradients may not be applicable, especially around a plasmonic hot spot (32). In fact, energetic carriers are excited primarily near plasmonic hot spots, and they are produced with an energy distribution that is not captured by the conventional TTM (Figure 1b). We term these energetic carriers produced immediately after plasmon decay nonthermal carriers because their distribution does not follow Fermi-Dirac statistics (see Section 2). These nonthermal carriers are believed to be the driving force for many plasmon-mediated photochemical reactions. Then, the short-lived nonthermal carriers relax within the electron subsystem (discussed in Section 3) and form a distribution that can be described by a Fermi-Dirac distribution at an elevated temperature, T_c (Figure 1c). We therefore term electrons in this distribution hot electrons, and they have been experimentally confirmed in thermionic emission experiments (33), among other studies (34-37). Note that many reports mix the usage of the terms nonthermal carriers and hot electrons, but for the clarity of this review, the definitions are as provided above. The hot electrons then relax by scattering with phonons to raise the lattice temperature, T_l , of the metal, resulting in photothermal heating (**Figure 1***d*). These microscopic thermalization steps are analyzed in more detail in this review on the basis of recent experimental studies.

2. NONRADIATIVE DECAY AND NONTHERMAL CARRIER GENERATION

Once excited, localized surface plasmons rapidly dissipate energy (approximately tens of femtoseconds) through either radiative channels (observed primarily as light scattering) or nonradiative channels (observed as light absorption) (39, 40). The efficiency of radiative and nonradiative decay scales with particle radius, R, as R^6 and R^3 , respectively (**Figure 1***a*); however, absorption still occurs in large plasmonic structures and constitutes the major factor limiting light-field confinement in sensing applications (7, 8). Therefore, we first focus on nonradiative decay, which has been historically regarded as parasitic absorption in the nanophotonics community (41) and which produces the characteristic nonthermal electron-hole pair distribution in the first tens of femtoseconds following plasmon excitation.

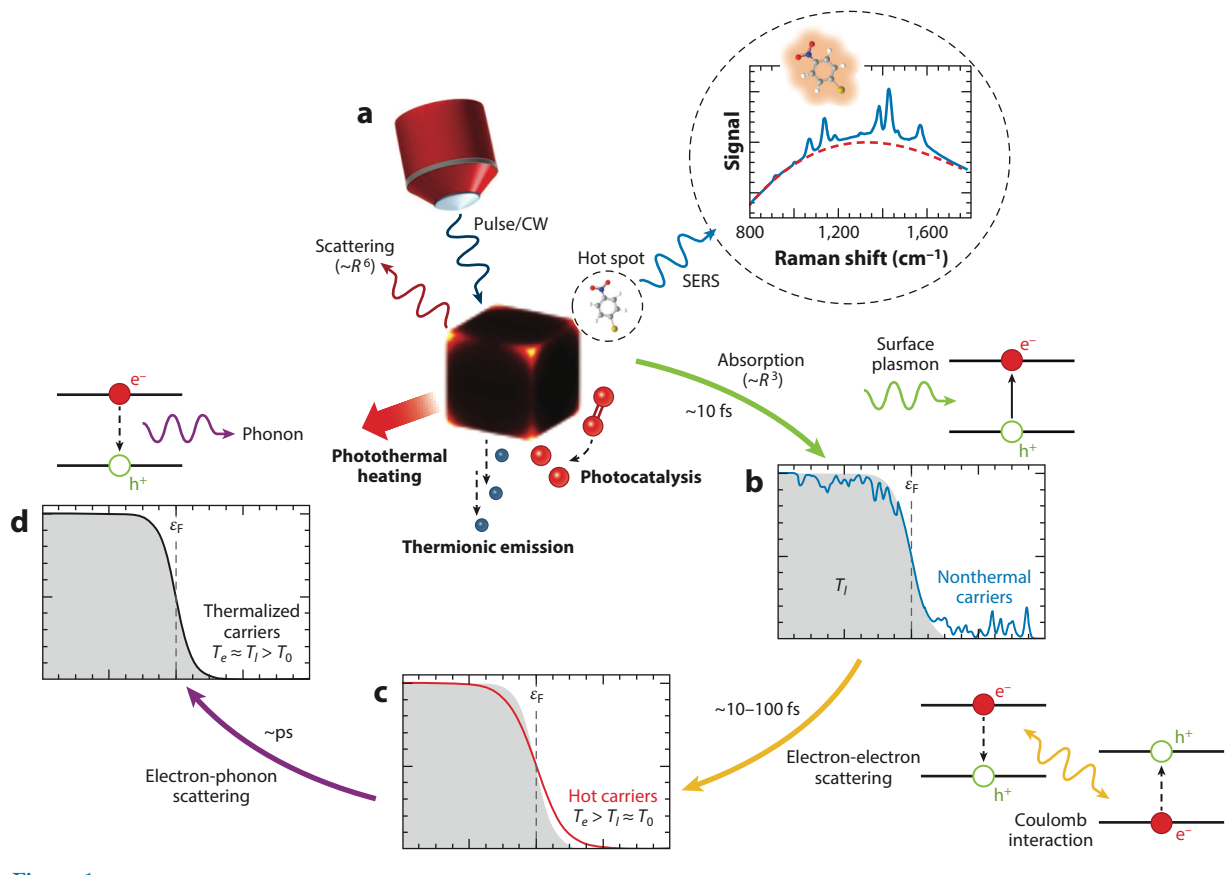
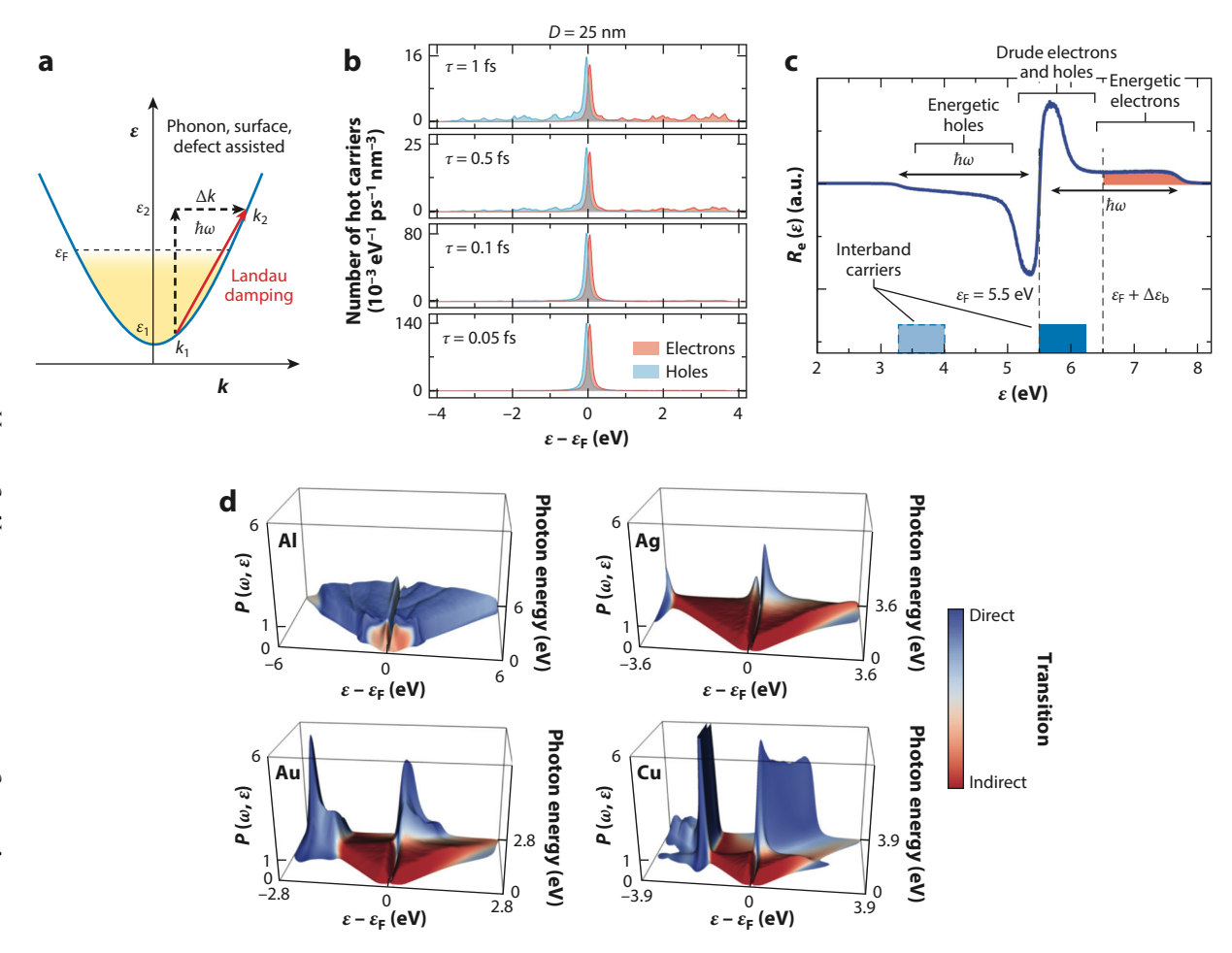


Figure 1

Schematic of plasmonic hot spots on a metal nanostructure and photothermalization of the plasmon-excited carriers. (a) Plasmonic hot spots (corners and edges) provide extreme light confinement and lead to improved sensitivity in SERS application. (Inset) The typical SERS spectrum of 4-NBT, a chemical widely studied in plasmonic catalysis. The red dashed line in the upper-right inset represents the SERS background. (b) Surface plasmons rapidly decay nonradiatively (absorption) into nonthermal electrons and holes within \sim 10 fs. Dephasing sets the upper limit for field concentration but also enables plasmon-mediated photocatalysis and photochemistry. (c) Nonthermal carriers redistribute energy through electron-electron scattering to form an ensemble of hot carriers with an elevated electronic temperature T_e that is greater than the temperature of lattice phonons T_e . The emission of hot carriers is observed in thermionic emission measurements. (d) Electron-phonon scattering mediates relaxation of hot carriers back to T_e , which is still greater than ambient temperature T_e , enabling photothermal applications. Figure adapted with permission from Reference 38. Abbreviations: 4-NBT, 4-nitrobenzenethil; CW, continuous wave; SERS, surface-enhanced Raman spectroscopy.

Analysis of an energy diagram in k-space can provide a simple physical picture of the non-radiative decay channel, or equivalently, the so-called Landau damping (**Figure 2**a). Collective electron density waves (i.e., plasmons) lose their coherent phase through the excitation of energetic electron-hole pairs, resulting in a direct transition between two states with different wave vectors, k_1 and k_2 (42). Strictly speaking, direct transitions between two free-electron-like states are prohibited by momentum conservation. Scattering with phonons, defects, or the nanoparticle surface can provide such momentum matching, such that a photon with energy $\hbar\omega = \varepsilon_2 - \varepsilon_1$ can be absorbed. Assuming that conservation of momentum is fulfilled, the generation rate and energy profile of nonthermal carriers have been calculated using Fermi's golden rule within a jellium model (43–47) or, equivalently, the quantum Liouville equation with the plasmon-induced

Figure 2



Schematic and theoretical insights into Landau damping of surface plasmons. (a) Landau damping, a direct transition between two states with different wave vectors, k_1 and k_2 . (b) Energy distribution and number density of generated nonthermal electrons (red lines) and holes (blue lines) calculated within a jellium model of a diameter D=25 nm silver nanosphere under resonant excitation ($\hbar\omega=3.65 \,\mathrm{eV}$). Longer relaxation time, τ , results in more energetic nonthermal carriers. Panel b adapted with permission from Reference 44. (c) The rate of carrier generation as a function of electronic energy for a localized plasmon wave in a gold nanosphere with radius R=4 nm excited at $\hbar\omega=2.2 \,\mathrm{eV}$. The two blue regions correspond to the intervals for generation of interband holes and electrons. Electrons with energy greater than the interfacial barrier $\Delta\varepsilon_b$ can be injected into surrounding material (red-shaded area). Panel c adapted with permission from Reference 51. (d) First-principles calculation of the energy distribution of hot carriers, $P(\omega,\varepsilon)$, generated by the decay of surface plasmons due to phonon-assisted and direct transitions, as a function of plasmon frequency (ω) and carrier energy (ε) in Al, Ag, Au, and Cu. The color scale indicates the relative contributions of phonon-assisted (red) and direct (blue) transitions. Panel d adapted with permission from Reference 53.

potential treated in its classical form (38, 48–52). This semiquantum method predicts that most of the nonthermal carriers are distributed within the vicinity of the Fermi level ε_F but that a small population of energetic electrons possess energy up to $\varepsilon_F + \hbar \omega$ (Figure 2*b,c*). It is indeed hypothesized that these energetic carriers enable unique nonthermal channels for energy and carrier transfer from plasmonic geometries into surrounding interfaces or chemical species.

However, as only the free-electron-like *sp*-band is considered, the aforementioned models are valid for intraband transitions but provide poor predictive power if the photon energy exceeds the interband threshold energy (4 eV for silver or 2.4 eV for gold). To explore the *d-sp* interband transition and, further, to understand contributions from phonon- or defect-assisted Landau damping, theoretical chemists have employed first-principles calculations (**Figure 2***d*). For instance, DFT+U (53, 54) and the GW approximation (where G stands for Green function, W is the screened Coulomb potential, and GW is the diagram employed for the electron self-energy) (55) have been combined with time-dependent density-functional theory (56). It is consistently found that the energy profile of nonthermal carriers is sensitive to the electronic band structure of the metal and the photon energy, $\hbar\omega$. In summary, interband transitions dominate if $\hbar\omega$ is above the interband threshold energy, and most of the plasmon energy decays as short-lived *d* holes. Below-threshold excitation, on the other hand, distributes the plasmon energy equally between nonthermal electrons and holes.

Significant experimental efforts have been devoted to providing direct or indirect evidence for the nonthermal carriers predicted by theory. Quantitative information such as the number density and energy distribution of nonthermal carriers has been provided by photoemission studies (57–59). In a photoemission measurement, impinging photons excite energetic, nonthermal electron-hole pairs in a material through Landau damping of the surface plasmon. Electrons that have sufficient energy to overcome the material's work function, as in photonenhanced thermionic emission (60), or that gain sufficient energy through multiple excitations, as in two-photon photoemission measurements, are emitted into the vacuum. The emitted electron emission yield and the energy distribution are measured. The distribution of photoemitted electrons from silver nanoparticles shows a broader, flat-band energy dependence compared with bulk films, with increased concentrations close to the Fermi level (59). This distribution agrees with the theory discussed above and is attributed to the thermalization of high-energy electrons with low-energy electrons through e-e scattering.

The perturbed electronic structure immediately after Landau damping also modifies the optical response of nanoparticles and thus can also be measured optically using ultrafast pump-probe transient spectroscopy (61–63). **Figure 3**b shows an ultrafast reflectivity measurement, wherein the perturbed electronic structure of a thin gold film is extracted from double inversion of the differential reflectivity $\Delta R/R$ through the Kramers–Kronig relation (61). Similarly, transient absorption studies of 2D arrays of gold nanoparticles have also been conducted, and an excellent correlation with the extended TTM (ETTM; discussed more in the next section) is achieved (62). Typically, the transient absorption spectrum displays a double exponential decay, in which shorter time constants (hundreds of femtoseconds) are attributed to the relaxation of nonthermal carriers through e-e scattering and longer time constants (longer than 1 ps) are attributed to the thermalization of electrons with the metal lattice via e-ph scattering. Across these experiments, the energy distribution of nonthermal carriers shows a relatively flat plateau, a feature associated with the intraband transition.

In addition to ultrafast measurements, the presence of nonthermal carriers that are produced during steady-state illumination has been measured on the basis of single-molecule transport studies (64). In these experiments a single-molecule junction is formed between a plasmonic gold film and the gold tip of a scanning tunneling microscope (**Figure 3**c). By modifying the applied bias and the highest occupied and lowest unoccupied molecular orbitals, one can photoelectrically probe the energy profile of nonthermal carriers during CW excitation. Indeed, the production of energetic nonthermal carriers in metals and their injection into molecules, even under relatively low-intensity CW illumination, are currently proposed as a primary mechanism underlying many plasmon-mediated photochemical reactions (9, 11, 12, 15, 65–69).

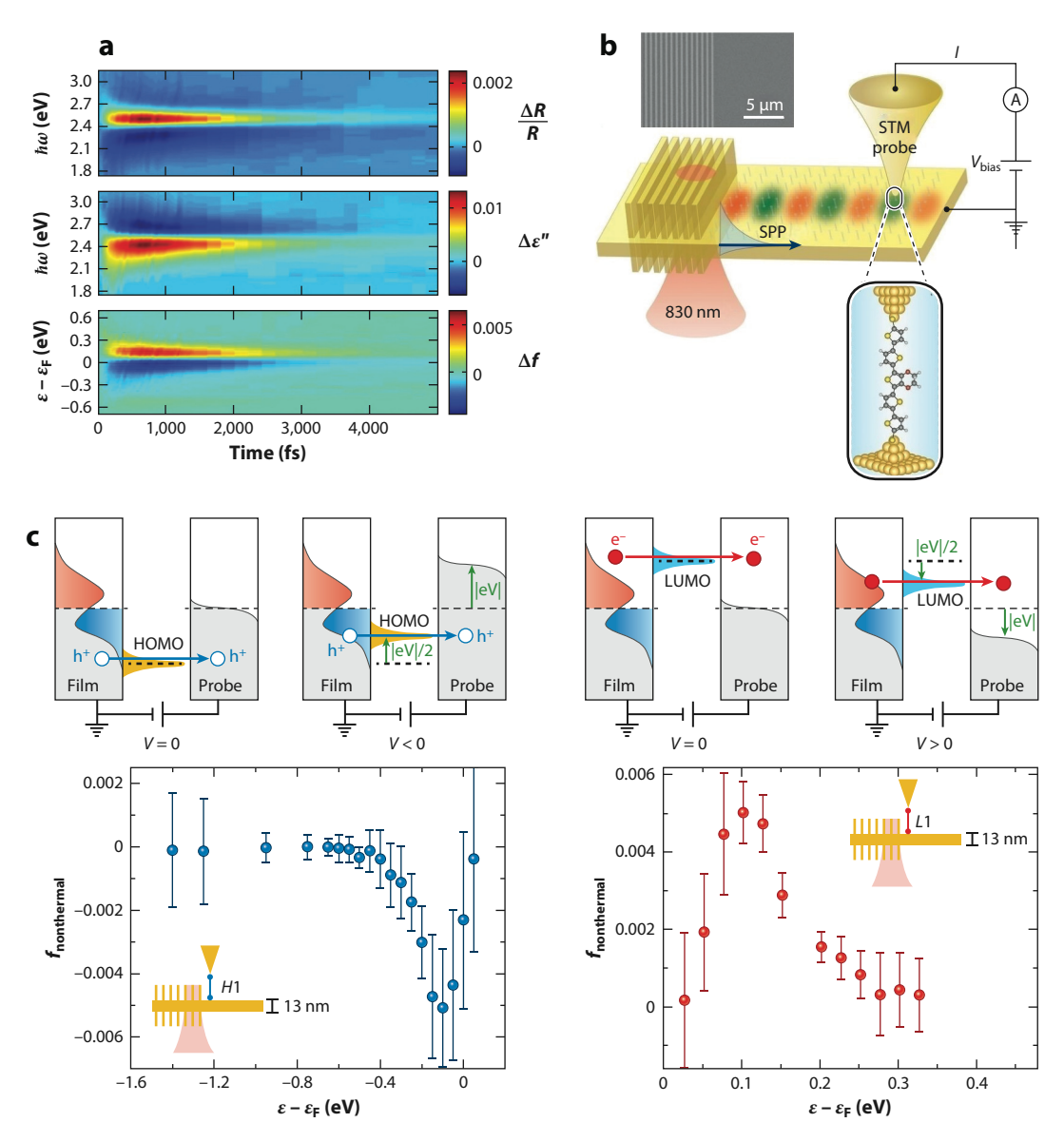


Figure 3

Ultrafast and steady-state measurements of plasmonic nonthermal carriers. (a) Inversion of experimental pump-probe data. Plots show the changes in reflectivity, dielectric function, and electron occupancy. Panel a adapted with permission from Reference 61. (b) Schematic of a single-molecule junction setup that probes nonthermal carriers generated from the decay of SPPs. SPPs are excited by illuminating a grating coupler with a 830-nm CW laser. (c, bottom) The measured nonthermal hole and electron distribution in a 13-nm gold film. (Top) A schematic of the frontier orbitals (HOMO and LUMO) of L1, a charge-transfer complex of quaterthiophene and tetracyanoethylene, and H1, 3,4-ethylenedioxythiophene, the two molecules used in the setup. Panels b and c adapted with permission from Reference 64. Abbreviations: CW, continuous wave; HOMO, highest occupied molecular orbital; LUMO, lowest unoccupied molecular orbital; SPP, surface plasmon polariton; STM, scanning tunneling microscope.

3. ELECTRON-ELECTRON SCATTERING AND HOT CARRIERS

In this section, we consider e-e scattering and discuss how the energy of the nonthermal carriers can be redistributed to form a pseudo-Fermi-Dirac distribution at an effective electronic temperature, T_c , that is significantly elevated compared with the lattice temperature of the metal—our explicit definition for the term hot carriers. We also discuss experimental evidence for hot carriers both during ultrafast pump-probe studies with large instantaneous optical pump power and during steady-state experiments with lower-intensity CW illumination.

The dynamics of carrier thermalization after Landau damping (Section 2) are commonly described with two distinct timescales: (a) a timescale of several hundred femtoseconds on which the electrons exchange energy among themselves through e-e scattering and (b) a longer timescale of \sim 1–2 ps on which the electron subsystem exchanges energy with the phonon subsystem through e-ph scattering. For nanoparticles placed in a chemically active environment, the phonon subsystem includes the bulk and surface phonons of the metal, as well as the phonons (vibrations) of the molecules adsorbed on or near the metal. Both e-e and e-ph scattering are dynamic processes; that is, the energy exchange via scattering is occurring whether the system is at equilibrium or out of equilibrium. Indeed, at equilibrium, the population and depopulation rates for electronic and phononic states are balanced, and the energy distributions are characterized with an equilibrium property (i.e., temperature).

However, when out of equilibrium, the energy contained among the nonthermal carriers produced via Landau damping is redistributed by e-e scattering events to provide the electron subsystem with an energy distribution that can be well described by an elevated pseudotemperature, T_e , that differs from the lattice (phonon) temperature, T_l . Then, the energy of the hot carriers flows into the phonon subsystem through e-ph scattering until the intersubsystem (electron and phonon) equilibrium is established. Though the e-e and e-ph scattering are continually occurring, the time required to establish the pseudoequilibrium in the electron subsystem is much less than the time required to establish the intersubsystem equilibrium. This disparity suggests decoupling of these two subsystems and leads to the well-known TTM (Equation 1), which is commonly used in ultrafast pump-probe measurements to study transient electron excitation and relaxation in bulk and nanoscale metals. The TTM assumes instantaneous thermalization of nonthermal electrons to hot electrons. This assumption, also known as the adiabatic assumption, however, is not in agreement with many experimental observations, when very short time delays (~100 fs) between the pump pulse and the probe pulse are used. To account for the nonthermal electron distribution, researchers have proposed the ETTM (Equation 2), in which the relaxation process is now divided into three interacting subsystems: the nonthermal carrier distribution, the hot carrier distribution, and the phonon subsystem. The major difference between the ETTM (Equation 2) and the TTM (Equation 1) is the accounting for the extremely short-lived (~100 fs) nonthermal carriers (Equation 2a),

$$\frac{\partial N}{\partial t} = -(\Gamma_{\text{e-e}} + \Gamma_{\text{e-ph}})N + S(r, t), \qquad 2a.$$

$$\frac{\partial (C_{\epsilon}T_{\epsilon})}{\partial t} = \nabla (k_{\epsilon}\nabla T_{\epsilon}) - G(T_{\epsilon} - T_{l}) + \Gamma_{e-e}N,$$
2b.

$$\frac{\partial (C_l T_l)}{\partial t} = \nabla (k_l \nabla T_l) + G(T_e - T_l) + \Gamma_{e-ph} N,$$
2c.

where N represents the energy density stored in the nonthermal carriers, and $\Gamma_{e-e}/\Gamma_{e-ph}$ is the energy loss rate to the hot electrons/phonon bath through e-e and e-ph scatterings, respectively.

In both the TTM and the ETTM, the heat conductivity term is commonly discarded assuming a homogeneous incident optical field and no spatial energy gradients within the nanostructure during photoexcitation. However, as we discuss more below, this assumption may not hold when plasmonic nanoparticles with optical hot spots are studied, especially during steady-state CW illumination. In Section 4, e-ph scattering is discussed in detail; here we focus on e-e scattering, which converts the nonthermal carrier distribution to a hot carrier distribution.

We first consider e-e scattering within the conduction band where the free-electron-like states and Fermi liquid theory can be applied, such that $\tau_{\rm e-e}^{-1}(\varepsilon) = K[(\pi k_B T_e)^2 + (\varepsilon - \varepsilon_{\rm F})^2]$, where K is the characteristic e-e scattering constant (70). When close to the Fermi level, the e-e scattering rate is comparable to the e-ph scattering rate; however, we still apply the TTM and leave the discussion of e-ph scattering for the next section. When the size of a nanostructure is reduced, K may become energy dependent if quantum size effects are relevant. Indeed, the e-e scattering rate has been determined by S-matrix methods that involve four electronic states (43). This exact approach is very time-consuming and thus the size of the nanoparticle is restricted to $\sim D < 6$ nm. The ee scattering matrix calculated from this exact approach shows energy dependence, and through parameterization, the scattering rates can be extrapolated to larger nanoparticles. Furthermore, carrier multiplication may also be observed during e-e scattering. That is, the population of electrons contained within some region of k-space is increased due to scattered electrons from other energy regions. Another way to evaluate the e-e scattering is to employ a screened interaction $W(r, r', \omega)$, which is the potential produced at r by a unit point charge placed at r' and oscillating with frequency ω . The method reduces the interacting electronic states from four to two (38); thus, the e-e scatterings in larger nanoparticles have been investigated this way. Alternatively, a so-called relaxation time approximation has also been used, in which it is assumed the nonthermal electrons relax to a Fermi–Dirac distribution, $f_{\rm FD}(\varepsilon, T_{\rm e})$, with a well-defined temperature $T_{\rm e}$ (71– 75). However, the relaxation time approximation assumes the collisions are elastic and isotropic and, like the TTM, also assumes homogeneous photoexcitation, so this picture is not applicable when inhomogeneous excitation occurs, for example, in nanostructures with hot spots.

Like the experimental measurements of nonthermal carriers, ultrafast pump-probe studies have been used to probe the dynamics of hot carriers at T_e (31, 32, 63, 76, 77). Based on geometry (e.g., bulk versus nanoscale), the instantaneous pump power density, and the thermal conductivity of the substrate, the reported hot electron temperature varies from several hundreds to thousands of Kelvin. However, the measured T_{ℓ} is based on relative changes in nonlinear transient signals that result from fluctuations of the electronic structure, such that the electrons that remain unchanged before and after pump excitation contribute no transient signal. Thus, important information about the actual size of the nonthermal or hot electrons that determines rates, efficiency, and yields in photochemistry and optoelectronic applications can be difficult to discern empirically. Further, in time-resolved experiments, it is usually implied that after an optical pulse all conduction electrons in a metal nanostructure thermalize through e-e scattering to reach a uniform, elevated T_{ε} before thermalizing with the lattice via e-ph scattering. However, this picture is at odds with steady-state CW illumination conditions, which necessarily produce sustained populations of nonthermal, hot (T_{ℓ}) , and thermalized (T_{ℓ}) electron distributions. In this latter steady-state scenario, determining the size of the nonequilibrium carrier populations is crucial in part because it is most comparable to conditions for plasmonic applications that intend to harvest solar energy.

In the steady state, Raman spectroscopy provides alternative thermometry and analysis techniques that can be used to address some of the limitations of conventional transient pump-probe spectroscopy (see Section 5). Historically, Raman spectroscopy and metallic nanoparticles are closely connected: (a) The confinement of light-field and near-field enhancement due to surface

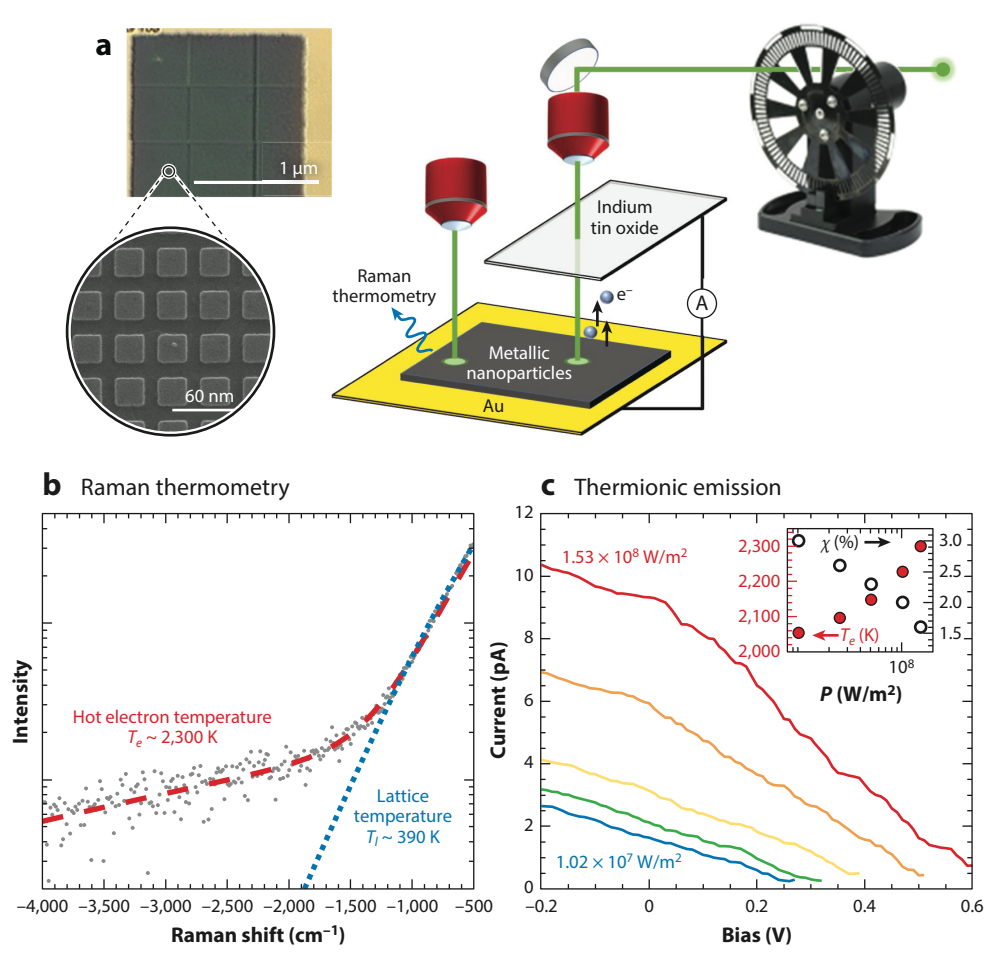


Figure 4

Methods for measuring the subpopulation of hot electrons in a steady state. (a) Schematic of an electronic Raman measurement (left) and a thermionic emission device (rigbt). A periodic array of gold nanocubes are fabricated on a smooth gold film using electron-beam lithography. The design maximizes optical absorption. A transparent, conducting indium tin oxide film on glass is a counter electrode for collecting the thermionically emitted electrons, detected using a lock-in amplification scheme. (b) Two-temperature Raman thermometry. The two slopes apparent in the anti-Stokes region indicate two temperature distributions within the nanostructure. (c) The I-V characteristics (colored lines) of a thermionic emission measurement. The short-circuit current and open-circuit voltage at each optical power uniquely define the temperature, T_e , and the fractional size, χ , of the population of hot electrons, as plotted in the inset. Figure adapted with permission from Reference 33.

plasmon resonances boosts the sensitivity of molecular Raman spectroscopy, giving rise to SERS, a technique that has been applied to analyze molecular analytes, even with single-molecule resolution (78); (b) it is also now well established that Raman spectroscopy can retrieve the temperature of metallic nanoparticles (**Figure 4a**). The inelastic light signal collected from plasmonic nanoparticles displays temperature-sensitive information in the anti-Stokes region (33, 37, 79–88). In brief, the slope of the anti-Stokes spectrum on a semilogarithmic plot is proportional to the temperature of the electron gas (**Figure 4b**) (for more discussion, see Section 5). Quantitative

thermometry has been demonstrated either through normalization to a reference spectrum (79, 80) or through careful consideration of the photonic density of states (33, 37, 85–88). If one analyzes the anti-Stokes spectral region over an energy bandwidth that extends to even higher energy under CW excitation between 107 and 1011 Wm⁻², a second slope is present, suggesting the existence of a second electronic population with an energetic distribution at a higher temperature (Figure 4b). Informed by the conventional TTM, we and other authors (33, 34, 37, 85, 86, 88) attribute these two slopes to the coexistence of two populations of electrons in the steady state: a small population (\sim 1%) of hot electrons at an elevated temperature T_e of ~103 to 104 K, and a larger population of electrons (~99%) thermalized with lattice phonons at T_l of ~ 1 to 100 K above room temperature. At first, this interpretation may seem unreasonable if one assumes homogeneous photoexcitation within the metal—a common assumption during analysis according to the TTM in time-resolved studies. For example, the predicted steady-state increase of T_e compared with T_l is only a few degrees under the CW conditions described above, according to Equation 1 (86). However, optical power is concentrated at hot spots in plasmonic nanoparticles, resulting in extremely inhomogeneous spatial excitation profiles, and there may be a preference for which electronic states participate in e-e scattering. That is, sustained spatial inhomogeneity and energy inhomogeneity during CW illumination could lead to the observed dual temperature behavior in the anti-Stokes signal.

To provide independent confirmation of the existence of sustained subpopulations of hot electrons at T_{ϵ} during CW illumination, we constructed a thermionic emission device. Hot electrons produced during photothermalization with kinetic energy greater than the metal work function are emitted across a vacuum gap (33). In our experiments, the excitation energy was lower than the work function of the metal so that direct photoemission via the photoelectric effect could be neglected. By analyzing the I-V characteristics of the photocurrent, we quantified the temperature distribution of the emitted electrons and the size of the electron population giving rise to the signal (**Figure 4c**). Very similar trends were observed in the Raman spectroscopic analysis under equivalent optical excitation conditions (see Section 5), confirming both the presence of hot carriers in the steady state and the interpretation of the inelastic Raman signal.

Other researchers have also reported hot carrier distributions at significantly elevated temperatures under steady-state illumination. For instance, Zenobi and coworkers (34) performed a similar Raman analysis in a scanning probe geometry and correlated the spectral signal of the hot electron temperature with surface chemical reactions that are inaccessible via thermal activation at the much lower lattice temperature. Link and coworkers (37) measured the anti-Stokes/Stokes (aS/S) ratio from individual gold nanorods, and their result yields elevated electronic distributions despite not using pulsed laser excitation. Hot carriers have also been probed in electrochemical cells. For example, Willets and coworkers (35) performed wavelength-dependent scanning electrochemical microscopy, and by choosing appropriate molecular probes (oxidation/reduction pairs), the observed hole distribution was described by an effective temperature of ~1,900 K when the electrochemical cell is illuminated at 1 W/cm². Hot electron injection from metal nanostructures into adjacent 2D materials also provides direct evidence of hot electron distributions (36).

The presence of superheated subpopulations of hot carriers during steady-state illumination is now clear based on many different lines of experimental evidence. Whether these observations contradict the timescales for hot carrier relaxation obtained from ultrafast studies depends on the spatial and energy inhomogeneity that can be sustained in nanostructures under CW illumination. Detailed insight into the actual mechanisms that provide energy inhomogeneity, as well as continued comparison with ultrafast experiments, is now required, especially for understanding the limits on the photochemical potential that can be obtained in plasmonic systems during solar energy harvesting.

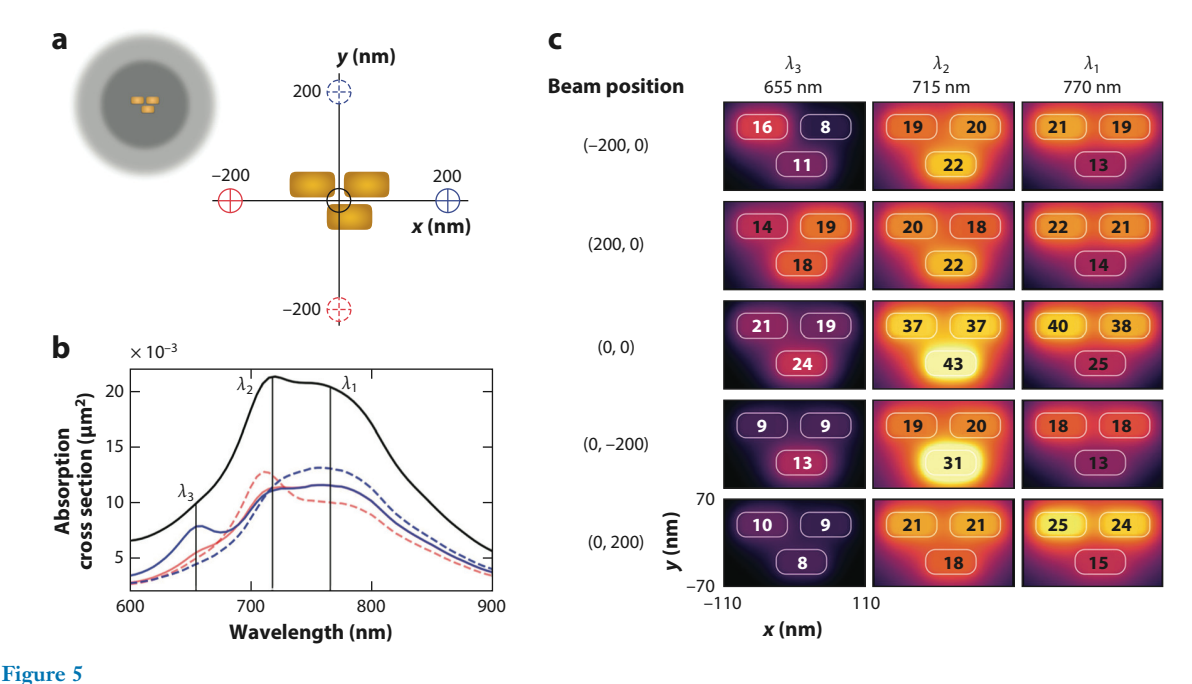
4. ELECTRON-PHONON SCATTERING

The electron and phonon subsystems are at equilibrium if nanostructures are kept in the dark, or after sufficiently long times (>1–10 ps) since pulse excitation. This equilibrium, similar to chemical equilibrium, is a dynamic process because the energy exchange between the electron and phonon subsystems is continually occurring but is balanced via e-ph scattering. For instance, heating nanoparticles on a laboratory hot plate could be considered a two-step process: (a) The energy of the phonon subsystem in metallic nanoparticles is increased because it receives thermal energy from the hot plate. This results in a transient scenario with $T_l > T_e = T_0$, where T_0 is the initial temperature. (b) The electron subsystem, almost instantaneously, extracts energy from the phonon subsystem through multiple e-ph scattering events and eventually reaches a new equilibrium with the phonon subsystem ($T_l = T_e > T_0$). Since electrons have extremely low mass compared with metallic lattice, the phonon-driven excitation of electrons is very fast, analogous to the Born–Oppenheimer approximation in quantum chemistry.

Conversely, the energy may also flow from the electron subsystem into the bulk and surface phonon subsystems, for instance, during the thermalization of plasmonic hot carriers. In the view of the electron subsystem, the energy input is the optical pulse (TTM; Equation 1) or the energy stored in nonthermal carriers (ETTM; Equation 2), and the output channel is the e-ph scattering into the phonon subsystem. Analogous to the formalism of detailed balance or to the Boltzmann equation (38, 74, 75), the effective electronic temperature, T_e , of hot carriers in the steady state is determined by the energy absorption and emission rates. The absorption rate (defined by the Landau damping and e-e scattering) is addressed in the previous sections. The emission rate is determined by e-ph scattering, which is commonly described with an empirical e-ph coupling constant, G (Equations 1 and 2). Similarly, in the view of the phonon subsystem, the lattice temperature, T_e , is determined by $G(T_e - T_e)$ and the energy dissipation rate to the environment.

Since the dissipation rate into the surroundings is dependent on the medium in which nanostructures are immersed, analysis of this environmental heat flow is beyond the scope of this review. Interested readers are referred to helpful review articles (89). However, once a geometry is fixed, the temperature of the electron and phonon subsystems is determined by G and the photon flux. For pure metals in vacuum, G is often regarded as an intrinsic property, but its quantified value in experiments may also depend on the nanoparticle size, lattice crystallinity, and the adsorbed surface species (77, 90–96). The measurement of G or τ_{e-ph} can be conducted by similar ultrafast studies such as those that quantify e-e scattering (77) or by temperature-dependent dark-field scattering spectroscopy (97, 98). Unlike e-e scattering, the e-ph scattering rate is relatively constant for all carriers within the sp-band (99). Therefore, instead of discussing results that quantify τ_{e-ph} , below we focus on the steady-state behavior of hot electrons thermalized with the lattice.

In either the TTM or the ETTM, the energy flow between the electron and phonon subsystems is proportional to $G(T_e - T_l)$. Therefore, determining the temperature difference, $T_e - T_l$, is equally as important as measuring G. Moreover, researchers are interested in measuring the lattice temperature of nanoparticles because it is intimately related to numerous photothermal applications, such as photothermal therapy (26–28, 100–102), thermal activation of chemical reactions and catalysts (19–21, 103, 104), photoacoustic imaging (22), and solar-thermal applications (25, 105, 106). Thermometry techniques that offer optical diffraction-limited resolution or better are discussed in detail in the next section. During steady-state illumination, T_l is not uniformly distributed within the absorbing geometry but rather is present with pronounced nanoscale temperature gradients (**Figure 5**), based on the modal structure that gives rise to localized optical energy concentration at hot spots (33, 37, 86, 107, 108).



rigure 3

Nanoscale temperature gradients probed by photothermal microscopy. (a) Illustration of the beam positions with respect to the position of the gold nanorod trimer in simulation. The colors and line styles of the crosshairs correspond to the absorption spectra in panel b. (b) Different absorption spectra resulting from the focused beams in panel a. When the beam is located at the dashed red or solid blue cross hairs, the λ_2 or λ_3 modes are strongly driven. (c) Heterodyne imaging resolves the steady-state temperature maps of the nanorod trimer. The numbers on three gold bricks list the temperatures in degrees Celsius above room temperature. Figure adapted with permission from Reference 108.

As an illustrative example, a simple heat transfer analysis (Equation 3) predicts the temperature rise of water containing a suspension of gold nanoshells approximately as $\Delta T(R_{\rm NP}) = \frac{V_{\rm NP}P_{\rm abs}}{4\pi k_0R_{\rm NP}} \approx 0.04 {\rm K}$ under sunlight, where $V_{\rm NP}$ and $R_{\rm NP}$ are the volume and radius of the nanoparticle, respectively, and $P_{\rm abs}$ is the absorbed power density. This minor predicted temperature rise contradicts experiments by Halas and coworkers (105), in which vapor generation is observed under incident sunlight. This discrepancy indeed reflects the nontrivial role of hot spots. The observed vaporization is attributed to extreme light trapping (i.e., the absorption of incident photons and scattered photons from nearby nanoparticles) into hot spots, and this highly localized heating generates a large temperature gradient at the nanoscale. This is important, because, as illustrated in the coupled differential Equations 1 and 3, the electron thermalization dynamics depend strongly on the local temperature of the lattice, so that nanoscale temperature gradients can result in the spatial inhomogeneity of hot electron temperature and population size. Therefore, the complex interrelated thermalization processes and thermal transport effects must be considered in parallel for understanding both the hot electron behavior and the vibrational heating,

$$\rho(\mathbf{r})C_{p}(\mathbf{r})\frac{\partial T(\mathbf{r},t)}{\partial t} = \nabla[\kappa(\mathbf{r})\nabla T(\mathbf{r},t)] + S(\mathbf{r},t).$$
3.

Here, $\rho(\mathbf{r})$ and $C_p(\mathbf{r})$ are the material density and lattice heat capacity, respectively. $S(\mathbf{r}, t)$ is the external source of heat, which is the amount of heat produced per unit time and volume in the nanostructure. Although difficult in practice without a more quantified understanding

of nanoscale heat transport effects, this simple heat flow model is compatible with a nonuniform temperature distribution that may result from an inhomogeneous heat generation rate or spatial-dependent thermal conductivity.

In fact, inhomogeneous photoexcitation and how it may result in inhomogeneous electronic temperature within the metal are not captured in most theoretical models, such as the TTM, in which a uniform photoexcitation is usually assumed. For instance, if we work within the framework of TTM and assume that the size of the hot electron population is ~1% of the electron bath (as we measured in Raman thermometry and the thermionic emission experiments) and that the rest of the electrons are thermalized with lattice in the steady state, we predict a moderate $T_e - T_l$ of only a few degrees, which is consistent with analysis provided in many other reports (74, 75, 82, 86). This prediction is obtained by multiplying the fractional hot electron population, χ , by the hot electron terms in the TTM (Equation 1) and setting the time dependence to zero (i.e., a steady state), $\chi C_e \frac{\partial T_e}{\partial t} = -\chi G(T_e - T_I) + P_{abs} = 0$. This simple analysis shows why it is not surprising that many theoretical approaches have difficulty rationalizing the magnitude of hot electron effects that are consistently reported in experiments (33, 35, 36). Further, given the challenges for a priori calculations of dynamic photothermalization processes in nanostructures, unresolved questions about nanoscale heat generation, vibrational coupling, transport, and interfacial thermal impedance are crucial for understanding both hot electrons and photothermal effects.

4.1. Coupling to Molecular Vibrations

So far, our discussion has been limited to analysis of electron-to-phonon thermalization that occurs within the nanostructure. Yet thermalization of nonthermal or hot electrons with external vibrational modes of, for example, adsorbed molecules is possible before equilibrium is established between electrons and lattice phonons within the metal. The analysis of isolated metal nanostructures, separate from their surroundings, is intuitive and a helpful starting approximation (38, 71, 74, 75). However, neglecting the possibility of energy transfer early in the thermalization process could be a factor in the ongoing debate regarding the role of hot electrons versus thermal (lattice) heating effects in plasmon-mediated photocatalysis (12, 15, 16, 65, 66, 71–75, 109–113). In fact, fast electron transfer from metals to adjacent semiconductors has been observed previously (94, 114), and more recently to adsorbed molecules by ultrafast Raman spectroscopies (115–117). We can therefore term this scattering between electrons in metals that are transferred to external molecular vibrational modes (phonons) external thermalization, and the detailed mechanisms behind it have been discussed in previous review articles (113, 118, 119).

In addition to external thermalization, direct coupling between plasmonic resonances and external vibrational modes has been a major development in the past few years, inspired in part by the study of cavity optomechanics (120, 121). The plasmonic particle is envisioned as a subwavelength optical cavity that can enhance light-matter interactions between optical and vibrational degrees of freedom either within the metal or with molecules located in the near field of the metal. This framework has provided alternative theoretical descriptions for SERS effects and distinct guidelines for optimizing SERS measurements (122, 123). Our laboratory (124) and other researchers (125–130) have been interested in the chemical implications of plasmonic systems that can promote vibrational strong coupling (131, 132). That is, when other damping pathways are minimized, the optical modes of a metal nanostructure can resonantly exchange energy with the vibrational modes of nearby molecules to form hybrid light-matter polaritonic eigenstates, fundamentally redefining the molecular orbital structure and potential energy landscape of the chemical system.

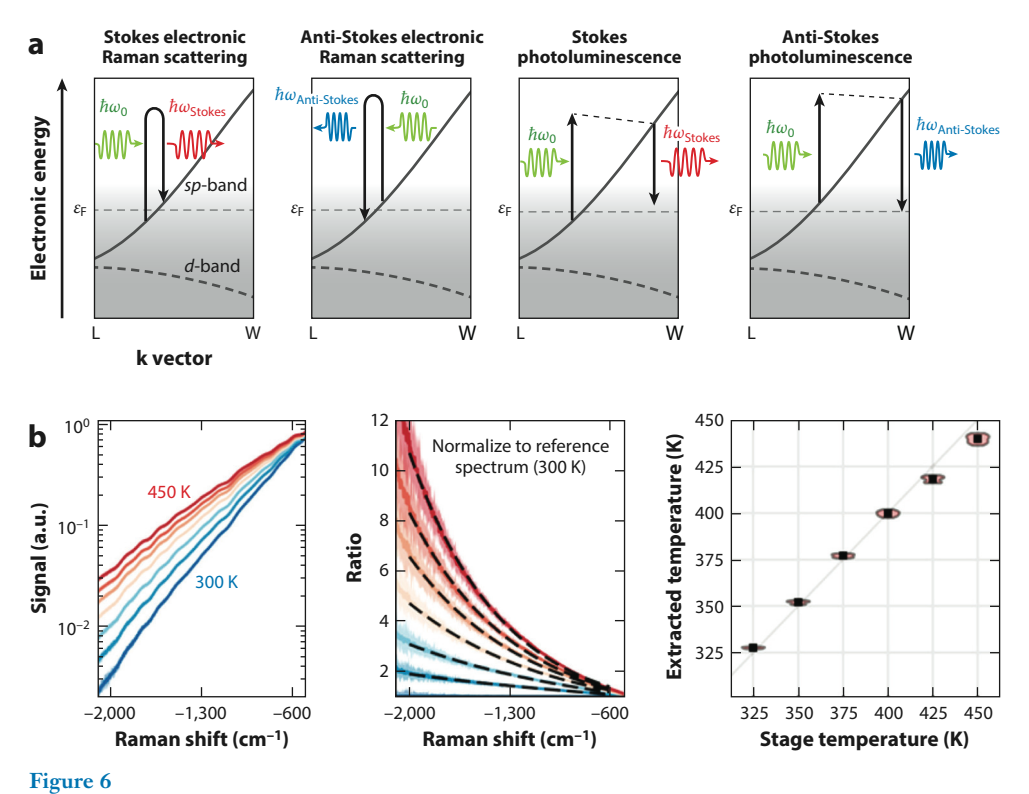
5. THERMOMETRY

In a thermometry measurement, a major goal is to determine the magnitude of temperature increases caused by photoexcitation and how thermal energy is distributed within a nanostructure or conducted into the surrounding environment. Historically, thermometry applications are dominated by optical spectroscopy techniques, though there has also been recent progress probing nanoscale temperature in plasmonic systems by electron microscopy (133, 134). There are two major classes of optical thermometry techniques, fluorescence thermometry and Raman thermometry, and both techniques are often performed at the single-nanoparticle level with optical diffraction-limited resolution. In a fluorescence thermometry measurement, the fluorescence emitted by a material is quantified in terms of, for example, intensity, polarization anisotropy, and lifetime (135, 136). Because these emission characteristics are usually temperature dependent, and due to the flexible choice of the fluorophores, fluorescence thermometry has been very popular in chemical and biological applications (137, 138). In addition to fluorescence and Raman thermometry, temperature gradients around a metal absorber can also be probed indirectly by measuring the temperature-dependent changes of surrounding media, most commonly manifest as thermal modulation of refractive index. For example, the nanoscale temperature gradient within gold nanorod dimers and trimers has been realized recently by photothermal heterodyne imaging (Figure 5). For a more detailed review on photothermal microscopy, see Orrit et al. (139).

Raman spectroscopy provides another major class of optical thermometry because the Raman signal is due to inelastic scattering of photons with phonons or vibrational modes and therefore is naturally connected to temperature (140). For instance, it is well established that the as/S ratio is proportional to $\exp[-bc\Delta v/k_BT]$, where Δv and T are the Raman shift and the measured temperature, respectively. This aS/S ratio methodology has been employed to analyze the temperature of molecular analytes on SERS substrates while presumably also providing information about the temperature of the underlying metal. However, several fundamental challenges impede conventional molecular aS/S thermometry when SERS enhancement is present (141). One major challenge is the large SERS background signal from the metal (142, 143), which shows clear temperature activation that is distinct from the temperature response of the analyte.

While it is possible to subtract the SERS background mathematically (144), more recent research has attempted to understand the underlying mechanism and to quantify temperature on the basis of the spectral analysis of the SERS background signal itself (33, 37, 82–87, 142, 145, 146). A recent review has summarized the major developments for this strategy (82), and the analysis of this signal has been a focus of research in our laboratory (33, 85, 86, 88). It is observed experimentally that, even in the absence of molecular adsorbates (84), a plasmonic metal shows a broad anti-Stokes and Stokes spectrum during monochromatic excitation with a clear dependence on the metal temperature, whether temperature is increased using a simple microscope stage heater or whether optical excitation is used to induce photothermalization. In general, the anti-Stokes spectral component increases in intensity at larger anti-Stokes energies when the sample is heated, suggesting that the signal is due to a thermally activated inelastic process that can be used to quantify the metal temperature. However, several questions about the signal are still unresolved, affecting the quantitative insight that can be achieved.

First, it is not clear what microscopic mechanisms give rise to the inelastic light (**Figure 6a**). Many studies suggest the signal is due to a coherent inelastic scattering process with the electron gas in the metal, termed spontaneous electronic Raman (83, 84, 146). Recent time-resolved experiments on silver nanoparticles identify coherent Fano interference between the metal signal and the molecular adsorbate vibrations, supporting a mechanism that would be most consistent with spontaneous electronic Raman (147). On the other hand, much experimental evidence points to photoluminescence upconversion from the metal (37, 73, 87). Although often negligible for



Inelastic light from plasmonic nanostructures reveals their temperature. (*a*) Proposed mechanisms for light–matter interactions leading to the inelastic signal from plasmonic nanoparticles: spontaneous electronic Raman versus photoluminescence. Panel *a* adapted with permission from Reference 82. (*b*) A normalization procedure for the anti-Stokes signal yields accurate temperature fitting. Panel *b* adapted with permission from Reference 148.

bulk metals, direct photoluminescence resulting from recombination of electron-hole pairs, like Raman processes, can be greatly enhanced based on the increased optical density of states supported by the plasmon resonance.

Second, although the signal is thermally activated, there is a debate about the appropriate population statistics underlying the spectral trend, with several different arguments put forth to justify Fermi–Dirac, Bose–Einstein, or Boltzmann distributions. Fitting the same spectrum to these different statistical distributions provides different estimates of the metal temperature, though these differences are often small compared with the experimental temperature resolution and less pronounced at higher temperatures (82). Additionally, many studies attempt fitting a statistical distribution only to the anti-Stokes spectrum (**Figure 6b**), as the temperature dependence of the Stokes spectrum shows less obvious thermally driven behavior. Nonetheless, excellent quantitative temperature correlation is observed when employing a Bose–Einstein distribution (79, 80, 148). Recently, we have developed a procedure for quantitatively fitting across the Stokes and anti-Stokes regions simultaneously based on Fermi–Dirac statistics (85). Our key assumption is that the observed spectrum during steady-state CW optical pumping results from contributions from both nonthermal and thermalized electron distributions in the metal (**Figure 7a**). We also observe excellent temperature correspondence while gaining additional insight about the plasmon dephasing process that generates the nonthermal electron distribution.

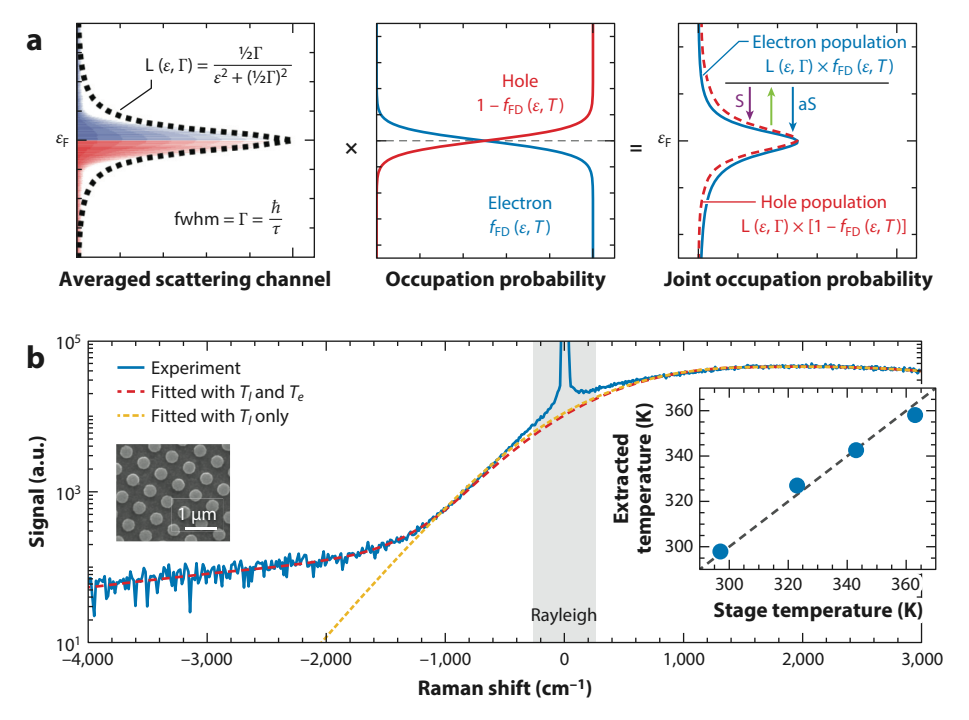


Figure 7

Proposed model to account for the inelastic light signal based on analysis of the joint density of states from thermal and nonthermal excitations. (a, left) The approximately Lorentzian nonthermal distribution accounts for all possible scattering events associated with plasmon dephasing, (middle) the thermal occupation probability, and (right) their product after multiplication: the joint density of states. (b) Fitting to a joint density of states, including two separate thermal distributions for T_e and T_l ($dashed\ red\ line$), matches well with experiment ($solid\ blue\ line$). The inset displays the quantitative agreement between fitted lattice temperature T_l and the thermal stage temperature. The samples used in this study were periodic arrays of gold nanodisks on a gold film. Figure adapted with permission from Reference 85. Abbreviation: fwhm, full width at half maximum.

The inelastic light signal from the metal can quantify temperature when the sample is on a heating stage and when the optical excitation is at a low fluence that minimizes perturbation of the metal's temperature. However, there is still debate about how to interpret the signal under conditions of more intense photoexcitation, pulsed or CW, that significantly heats the metal via photothermalization. As discussed above, under CW excitation between 10^7 and 10^{11} W/m² the anti-Stokes signal characteristically displays two distinct exponential regions, for example, two different linear slopes on a logarithmic intensity axis (**Figure 7b**), at higher (-4,000 to -1,500 cm $^{-1}$) and lower (-1,200 to -200 cm $^{-1}$) anti-Stokes energies. We interpret these trends as indicative of the two different electronic temperatures described in the TTM, with the hot electron temperature 1,000-2,000 K greater than the temperature of the electrons thermalized with the metal lattice, which also increases to 500-600 K based on the fitting described above. We note that the possible involvement of the interband transition has also been hypothesized to cause a second slope as reported by Orrit et al. (149), though in that case the functional form of the spectrum is distinct from a thermal distribution.

Furthermore, we note that the inelastic light signal is received predominantly from regions of the nanostructure that have the most optical field enhancement, as in all SERS measurements, and consequently where there is the most extreme energy confinement. That is, the signal is only representative of the hottest plasmonic hot spots (150). It is still unclear how that energy is distributed throughout the nanoscale geometry. Indeed, a recent report from the Frontiera lab (115) analyzed the time-resolved thermal activation of molecular analytes on plasmonic metal surfaces during optical pumping, observing very low transfer of thermal energy across the metal surface into adsorbed molecules. Thus, there continues to be a crucial need to further develop strategies to gain better insight into the temperature and energy distribution within individual plasmonic absorbers and into how energy is transmitted into the surrounding environment.

6. SUMMARY AND OUTLOOK

What is the fundamental difference between photothermalization in plasmonic nanostructures in a steady state and pulse excitation? By analyzing several recent studies, we offer a preliminary answer: the coexistence of sustained populations of nonthermal, hot, and thermalized electrons. This unique carrier distribution seems to be associated most likely with pronounced energy gradients at plasmonic hot spots. Yet confirming spatial inhomogeneity is challenging and deserves attention in the still-evolving field of plasmon-mediated applications, especially photocatalysis. Possible avenues for future study are the use of time-resolved spectroscopies combined with subdiffraction-limited spatial resolution, the refinement of thermometry techniques that can quantify temperature gradients around individual plasmonic hotpots, and the development of theoretical methods that are compatible with the anisotropic energy density inside a nanostructure.

Although confirmation of the underlying physical mechanism of inelastic light emission from plasmonic metals (i.e., the SERS background) is still pending, spectral analysis of the signal can give deep insight into photothermalization for both time-resolved and steady-state experiments. There is currently limited experimental effort dedicated to distinguishing whether the signal is due to electronic Raman or photoluminescence. However, developing a more refined understanding of such light emission will lead to an even more robust tool to scrutinize photothermalization mechanisms and will likely aid the multidisciplinary fields studying plasmon-mediated photochemistry. We suggest future experiments that analyze the power dependence, spectral dependence, or the coherent timescales of the signal, for which mechanisms based on electronic Raman or photoluminescence are expected to result in quite different behavior.

DISCLOSURE STATEMENT

The authors are not aware of any affiliation, memberships, funding, or financial holdings that might be perceived as affecting the objectivity of this review.

ACKNOWLEDGMENTS

This work was funded in part by the National Science Foundation (grant CHE-2108288). M.S. also acknowledges support from the Welch Foundation (A-1886).

LITERATURE CITED

- Kelly KL, Coronado E, Zhao LL, Schatz GC. 2003. The optical properties of metal nanoparticles: the influence of size, shape, and dielectric environment. J. Phys. Chem. B 107:668–77
- 2. Hartland GV. 2011. Optical studies of dynamics in noble metal nanostructures. Chem. Rev. 111:3858–87
- Langer J, Jimenez de Aberasturi D, Aizpurua J, Alvarez-Puebla RA, Auguié B, et al. 2020. Present and future of surface-enhanced Raman scattering. ACS Nano 14:28–117

- Han XX, Rodriguez RS, Haynes CL, Ozaki Y, Zhao B. 2022. Surface-enhanced Raman spectroscopy. Nat. Rev. Methods Primers 1:87
- Bell SEJ, Charron G, Cortés E, Kneipp J, de la Chapelle ML, et al. 2020. Towards reliable and quantitative surface-enhanced Raman scattering (SERS): from key parameters to good analytical practice. *Angew. Chem. Int. Ed.* 59:5454–62
- Zhu W, Esteban R, Borisov AG, Baumberg JJ, Nordlander P, et al. 2016. Quantum mechanical effects in plasmonic structures with subnanometre gaps. Nat. Commun. 7:11495
- Khurgin JB, Sun G. 2017. Landau damping—the ultimate limit of field confinement and enhancement in plasmonic structures. In *Quantum Plasmonics*, ed. SI Bozhevolnyi, L Martin-Moreno, F Garcia-Vidal, pp. 303–22. Cham, Switz.: Springer Int. Publ.
- Khurgin J, Tsai W-Y, Tsai DP, Sun G. 2017. Landau damping and limit to field confinement and enhancement in plasmonic dimers. ACS Photon. 4:2871–80
- Linic S, Chavez S, Elias R. 2021. Flow and extraction of energy and charge carriers in hybrid plasmonic nanostructures. Nat. Mater. 20:916–24
- Aslam U, Rao VG, Chavez S, Linic S. 2018. Catalytic conversion of solar to chemical energy on plasmonic metal nanostructures. Nat. Catal. 1:656–65
- Aslam U, Chavez S, Linic S. 2017. Controlling energy flow in multimetallic nanostructures for plasmonic catalysis. Nat. Nanotechnol. 12:1000–5
- Zhou L, Lou M, Bao JL, Zhang C, Liu JG, et al. 2021. Hot carrier multiplication in plasmonic photocatalysis. PNAS 118:e2022109118
- 13. Zhou L, Martirez JMP, Finzel J, Zhang C, Swearer DF, et al. 2020. Light-driven methane dry reforming with single atomic site antenna-reactor plasmonic photocatalysts. *Nat. Energy* 5:61–70
- Robatjazi H, Bao JL, Zhang M, Zhou L, Christopher P, et al. 2020. Plasmon-driven carbon-fluorine (C(sp³)-F) bond activation with mechanistic insights into hot-carrier-mediated pathways. Nat. Catal. 3:564-73
- Zhou L, Swearer DF, Zhang C, Robatjazi H, Zhao H, et al. 2018. Quantifying hot carrier and thermal contributions in plasmonic photocatalysis. Science 362:69–72
- Zhan C, Moskovits M, Tian Z-Q. 2020. Recent progress and prospects in plasmon-mediated chemical reaction. *Matter* 3:42–56
- Zhu Y, Xu H, Yu P, Wang Z. 2021. Engineering plasmonic hot carrier dynamics toward efficient photodetection. Appl. Phys. Rev. 8:021305
- Knight MW, Sobhani H, Nordlander P, Halas NJ. 2011. Photodetection with active optical antennas. Science 332:702–4
- Dhiman M, Maity A, Das A, Belgamwar R, Chalke B, et al. 2019. Plasmonic colloidosomes of black gold for solar energy harvesting and hotspots directed catalysis for CO₂ to fuel conversion. *Chem. Sci.* 10:6594–603
- Luo S, Ren X, Lin H, Song H, Ye J. 2021. Plasmonic photothermal catalysis for solar-to-fuel conversion: current status and prospects. *Chem. Sci.* 12:5701–19
- Zhang F, Li Y-H, Qi M-Y, Yamada YMA, Anpo M, et al. 2021. Photothermal catalytic CO₂ reduction over nanomaterials. Chem. Catal. 1:272–97
- Gellini C, Feis A. 2021. Optothermal properties of plasmonic inorganic nanoparticles for photoacoustic applications. *Photoacoustics* 23:100281
- Challener WA, Peng C, Itagi AV, Karns D, Peng W, et al. 2009. Heat-assisted magnetic recording by a near-field transducer with efficient optical energy transfer. *Nat. Photon.* 3:220–24
- 24. O'Connor D, Zayats AV. 2010. The third plasmonic revolution. Nat. Nanotechnol. 5:482-83
- Baffou G, Cichos F, Quidant R. 2020. Applications and challenges of thermoplasmonics. Nat. Mater. 19:946–58
- Cole JR, Mirin NA, Knight MW, Goodrich GP, Halas NJ. 2009. Photothermal efficiencies of nanoshells and nanorods for clinical therapeutic applications. 7. Phys. Chem. C 113:12090–94
- Bucharskaya AB, Khlebtsov NG, Khlebtsov BN, Maslyakova GN, Navolokin NA, et al. 2022. Photothermal and photodynamic therapy of tumors with plasmonic nanoparticles: challenges and prospects.
 Materials 15:1606

- Ali MRK, Wu Y, El-Sayed MA. 2019. Gold-nanoparticle-assisted plasmonic photothermal therapy advances toward clinical application. J. Phys. Chem. C 123:15375–93
- 29. Kauranen M, Zayats AV. 2012. Nonlinear plasmonics. Nat. Photon. 6:737-48
- Panoiu NC, Sha WEI, Lei DY, Li GC. 2018. Nonlinear optics in plasmonic nanostructures. J. Opt. 20:083001
- Singh N. 2010. Two-temperature model of nonequilibrium electron relaxation: a review. Int. J. Mod. Phys. B 24:1141–58
- Bresson P, Bryche JF, Besbes M, Moreau J, Karsenti PL, et al. 2020. Improved two-temperature modeling of ultrafast thermal and optical phenomena in continuous and nanostructured metal films. *Phys. Rev.* B 102:155127
- Wu S, Hogan N, Sheldon M. 2019. Hot electron emission in plasmonic thermionic converters. ACS Energy Lett. 4:2508–13
- Szczerbiński J, Gyr L, Kaeslin J, Zenobi R. 2018. Plasmon-driven photocatalysis leads to products known from e-beam and X-ray-induced surface chemistry. Nano Lett. 18:6740–49
- Yu Y, Wijesekara KD, Xi X, Willets KA. 2019. Quantifying wavelength-dependent plasmonic hot carrier energy distributions at metal/semiconductor interfaces. ACS Nano 13:3629–37
- Li L, Shao L, Liu X, Gao A, Wang H, et al. 2020. Room-temperature valleytronic transistor. Nat. Nanotechnol. 15:743–49
- Cai Y-Y, Sung E, Zhang R, Tauzin LJ, Liu JG, et al. 2019. Anti-Stokes emission from hot carriers in gold nanorods. Nano Lett. 19:1067–73
- Saavedra JRM, Asenjo-Garcia A, García de Abajo FJ. 2016. Hot-electron dynamics and thermalization in small metallic nanoparticles. ACS Photon. 3:1637–46
- 39. Maier SA. 2007. Plasmonics: Fundamentals and Applications. Berlin: Springer Science & Business Media
- Kreibig U, Vollmer M. 2013. Optical Properties of Metal Clusters. Berlin: Springer Science & Business Media
- 41. Khurgin JB. 2015. How to deal with the loss in plasmonics and metamaterials. Nat. Nanotechnol. 10:2-6
- 42. Kawabata A, Kubo R. 1966. Electronic properties of fine metallic particles. II. Plasma resonance absorption. 7. Phys. Soc. 7pn. 21:1765–72
- Liu JG, Zhang H, Link S, Nordlander P. 2018. Relaxation of plasmon-induced hot carriers. ACS Photon. 5:2584–95
- Manjavacas A, Liu JG, Kulkarni V, Nordlander P. 2014. Plasmon-induced hot carriers in metallic nanoparticles. ACS Nano 8:7630–38
- Dal Forno S, Ranno L, Lischner J. 2018. Material, size, and environment dependence of plasmoninduced hot carriers in metallic nanoparticles. J. Phys. Chem. C 122:8517–27
- Kumarasinghe CS, Premaratne M, Bao Q, Agrawal GP. 2015. Theoretical analysis of hot electron dynamics in nanorods. Sci. Rep. 5:12140
- Kornbluth M, Nitzan A, Seideman T. 2013. Light-induced electronic non-equilibrium in plasmonic particles. J. Chem. Phys. 138:174707
- Govorov AO, Zhang H, Gun'ko YK. 2013. Theory of photoinjection of hot plasmonic carriers from metal nanostructures into semiconductors and surface molecules. 7. Phys. Chem. C 117:16616–31
- Hartland GV, Besteiro LV, Johns P, Govorov AO. 2017. What's so hot about electrons in metal nanoparticles? ACS Energy Lett. 2:1641–53
- Zhang H, Govorov AO. 2014. Optical generation of hot plasmonic carriers in metal nanocrystals: the effects of shape and field enhancement. *7. Phys. Chem. C* 118:7606–14
- Besteiro LV, Kong X-T, Wang Z, Hartland G, Govorov AO. 2017. Understanding hot-electron generation and plasmon relaxation in metal nanocrystals: quantum and classical mechanisms. ACS Photon. 4:2759–81
- 52. Govorov AO, Zhang H. 2015. Kinetic density functional theory for plasmonic nanostructures: breaking of the plasmon peak in the quantum regime and generation of hot electrons. *7. Phys. Chem. C* 119:6181–94
- Brown AM, Sundararaman R, Narang P, Goddard WA 3rd, Atwater HA. 2016. Nonradiative plasmon decay and hot carrier dynamics: effects of phonons, surfaces, and geometry. ACS Nano 10:957–66
- Sundararaman R, Narang P, Jermyn AS, Goddard WA 3rd, Atwater HA. 2014. Theoretical predictions for hot-carrier generation from surface plasmon decay. Nat. Commun. 5:5788

- Bernardi M, Mustafa J, Neaton JB, Louie SG. 2015. Theory and computation of hot carriers generated by surface plasmon polaritons in noble metals. *Nat. Commun.* 6:7044
- 56. Zhang Y. 2021. Theory of plasmonic hot-carrier generation and relaxation. 7. Phys. Chem. A 125:9201-8
- Zhu XY. 2002. Electron transfer at molecule-metal interfaces: a two-photon photoemission study. Annu. Rev. Phys. Chem. 53:221–47
- Berglund CN, Spicer WE. 1964. Photoemission studies of copper and silver: experiment. Phys. Rev. 136:A1044–64
- Evers F, Rakete C, Watanabe K, Menzel D, Freund H-J. 2005. Two-photon photoemission from silver nanoparticles on thin alumina films: role of plasmon excitation. Surface Sci. 593:43

 –48
- Schwede JW, Bargatin I, Riley DC, Hardin BE, Rosenthal SJ, et al. 2010. Photon-enhanced thermionic emission for solar concentrator systems. *Nat. Mater.* 9:762–67
- Heilpern T, Manjare M, Govorov AO, Wiederrecht GP, Gray SK, Harutyunyan H. 2018. Determination of hot carrier energy distributions from inversion of ultrafast pump-probe reflectivity measurements. *Nat. Commun.* 9:1853
- O'Keeffe P, Catone D, Di Mario L, Toschi F, Magnozzi M, et al. 2021. Disentangling the temporal dynamics of nonthermal electrons in photoexcited gold nanostructures. *Laser Photon. Rev.* 15:2100017
- Sun CK, Vallée F, Acioli LH, Ippen EP, Fujimoto JG. 1994. Femtosecond-tunable measurement of electron thermalization in gold. Phys. Rev. B 50:15337

 –48
- Reddy H, Wang K, Kudyshev Z, Zhu L, Yan S, et al. 2020. Determining plasmonic hot-carrier energy distributions via single-molecule transport measurements. Science 369:423–26
- Mukherjee S, Zhou L, Goodman AM, Large N, Ayala-Orozco C, et al. 2014. Hot-electron-induced dissociation of H₂ on gold nanoparticles supported on SiO₂. J. Am. Chem. Soc. 136:64–67
- Mukherjee S, Libisch F, Large N, Neumann O, Brown LV, et al. 2013. Hot electrons do the impossible: plasmon-induced dissociation of H₂ on Au. Nano Lett. 13:240–47
- Linic S, Aslam U, Boerigter C, Morabito M. 2015. Photochemical transformations on plasmonic metal nanoparticles. Nat. Mater. 14:567–76
- Linic S, Christopher P, Ingram DB. 2011. Plasmonic-metal nanostructures for efficient conversion of solar to chemical energy. Nat. Mater. 10:911–21
- Christopher P, Xin H, Linic S. 2011. Visible-light-enhanced catalytic oxidation reactions on plasmonic silver nanostructures. Nat. Chem. 3:467–72
- 70. Coleman P. 2015. Introduction to Many-Body Physics. Cambridge, UK: Cambridge Univ. Press
- Sivan Y, Un IW, Dubi Y. 2019. Assistance of metal nanoparticles in photocatalysis nothing more than a classical heat source. Fanday Discuss. 214:215–33
- Dubi Y, Un IW, Sivan Y. 2022. Distinguishing thermal from nonthermal ("hot") carriers in illuminated molecular junctions. *Nano Lett.* 22:2127–33
- 73. Sivan Y, Dubi Y. 2021. Theory of "hot" photoluminescence from Drude metals. ACS Nano 15:8724-32
- Dubi Y, Un IW, Sivan Y. 2020. Thermal effects an alternative mechanism for plasmon-assisted photocatalysis. Chem. Sci. 11:5017–27
- Dubi Y, Sivan Y. 2019. "Hot" electrons in metallic nanostructures-non-thermal carriers or heating? Light Sci. Appl. 8:89
- Jiang L, Tsai H-L. 2004. An improved two-temperature model for metal thin film heating by femtosecond laser pulses. Int. Congr. Appl. Lasers Electro-Opt. 2004:M602
- Block A, Liebel M, Yu R, Spector M, Sivan Y, et al. 2019. Tracking ultrafast hot-electron diffusion in space and time by ultrafast thermomodulation microscopy. Sci. Adv. 5:eaav8965
- Nie S, Emory SR. 1997. Probing single molecules and single nanoparticles by surface-enhanced Raman scattering. Science 275:1102–6
- Huang J, Wang W, Murphy CJ, Cahill DG. 2014. Resonant secondary light emission from plasmonic Au nanostructures at high electron temperatures created by pulsed-laser excitation. PNAS 111:906–11
- Xie X, Cahill DG. 2016. Thermometry of plasmonic nanostructures by anti-Stokes electronic Raman scattering. Appl. Phys. Lett. 109:183104
- Carattino A, Caldarola M, Orrit M. 2018. Gold nanoparticles as absolute nanothermometers. Nano Lett. 18:874–80

- 82. Baffou G. 2021. Anti-Stokes thermometry in nanoplasmonics. ACS Nano 15:5785-92
- Mertens J, Kleemann M-E, Chikkaraddy R, Narang P, Baumberg JJ. 2017. How light is emitted by plasmonic metals. Nano Lett. 17:2568–74
- Hugall JT, Baumberg JJ. 2015. Demonstrating photoluminescence from Au is electronic inelastic light scattering of a plasmonic metal: the origin of SERS backgrounds. Nano Lett. 15:2600–4
- 85. Wu S, Cheng OH-C, Zhao B, Hogan N, Lee A, et al. 2021. The connection between plasmon decay dynamics and the surface enhanced Raman spectroscopy background: inelastic scattering from non-thermal and hot carriers. *J. Appl. Phys.* 129:173103
- Hogan N, Wu S, Sheldon M. 2020. Photothermalization and hot electron dynamics in the steady state.
 Phys. Chem. C 124:4931–45
- 87. Cai Y-Y, Liu JG, Tauzin LJ, Huang D, Sung E, et al. 2018. Photoluminescence of gold nanorods: Purcell effect enhanced emission from hot carriers. ACS Nano 12:976–85
- Hogan N, Sheldon M. 2020. Comparing steady state photothermalization dynamics in copper and gold nanostructures. 7. Chem. Phys. 152:061101
- Jauffred L, Samadi A, Klingberg H, Bendix PM, Oddershede LB. 2019. Plasmonic heating of nanostructures. Chem. Rev. 119:8087–130
- 90. Huang W, Qian W, El-Sayed MA, Ding Y, Wang ZL. 2007. Effect of the lattice crystallinity on the electron–phonon relaxation rates in gold nanoparticles. *7. Phys. Chem. C* 111:10751–57
- 91. Del Fatti V, Langot P, Vallée F. 2002. *Electron-phonon scattering in metal clusters: size effects.* Paper presented at the Quantum Electronics and Laser Science Conference, Long Beach, CA, May 19–22
- Singh N. 2004. Hot electron relaxation in a metal nanoparticle: electron surface-phonon interaction. Mod. Phys. Lett. B 18:1261–65
- 93. Arbouet A, Voisin C, Christofilos D, Langot P, Fatti ND, et al. 2003. Electron-phonon scattering in metal clusters. *Phys. Rev. Lett.* 90:177401
- Tagliabue G, DuChene JS, Abdellah M, Habib A, Gosztola DJ, et al. 2020. Ultrafast hot-hole injection modifies hot-electron dynamics in Au/p-GaN heterostructures. Nat. Mater. 19:1312–18
- Hodak J, Martini I, Hartland GV. 1998. Ultrafast study of electron-phonon coupling in colloidal gold particles. Chem. Phys. Lett. 284:135–41
- 96. Mongin D, Maioli P, Burgin J, Langot P, Cottancin E, et al. 2019. Ultrafast electron-lattice thermalization in copper and other noble metal nanoparticles. *7. Phys. Condens. Matter* 31:084001
- Jiang W, Hu H, Deng Q, Zhang S, Xu H. 2020. Temperature-dependent dark-field scattering of single plasmonic nanocavity. *Nanophotonics* 9:3347–56
- Konrad A, Wackenhut F, Hussels M, Meixner AJ, Brecht M. 2013. Temperature dependent luminescence and dephasing of gold nanorods. J. Phys. Chem. C 117:21476–82
- Gieseking RL, Ratner MA, Schatz GC. 2016. Review of plasmon-induced hot-electron dynamics and related SERS chemical effects. In *Frontiers of Plasmon Enhanced Spectroscopy*, ed. Y Ozaki, GC Schatz, D Graham, T Itoh, pp. 1–22. Washington, DC: Am. Chem. Soc.
- Lal S, Clare SE, Halas NJ. 2008. Nanoshell-enabled photothermal cancer therapy: impending clinical impact. Acc. Chem. Res. 41:1842–51
- Turcheniuk K, Dumych T, Bilyy R, Turcheniuk V, Bouckaert J, et al. 2016. Plasmonic photothermal cancer therapy with gold nanorods/reduced graphene oxide core/shell nanocomposites. RSC Adv. 6:1600–10
- Nasseri B, Alizadeh E, Bani F, Davaran S, Akbarzadeh A, et al. 2022. Nanomaterials for photothermal and photodynamic cancer therapy. Appl. Phys. Rev. 9:011317
- 103. Grote R, Habets R, Rohlfs J, Sastre F, Meulendijks N, et al. 2020. Collective photothermal effect of Al₂O₃-supported spheroidal plasmonic Ru nanoparticle catalysts in the sunlight-powered Sabatier reaction. ChemCatChem 12:5618–22
- 104. Liu T, Li Y. 2016. Plasmonic solar desalination. Nat. Photon. 10:361–62
- Neumann O, Urban AS, Day J, Lal S, Nordlander P, Halas NJ. 2013. Solar vapor generation enabled by nanoparticles. ACS Nano 7:42–49
- Boriskina SV, Ghasemi H, Chen G. 2013. Plasmonic materials for energy: from physics to applications. *Mater. Today* 16:375–86

- Bhattacharjee U, West CA, Hosseini Jebeli SA, Goldwyn HJ, Kong X-T, et al. 2019. Active far-field control of the thermal near-field via plasmon hybridization. ACS Nano 13:9655–63
- Hosseini Jebeli SA, West CA, Lee SA, Goldwyn HJ, Bilchak CR, et al. 2021. Wavelength-dependent photothermal imaging probes nanoscale temperature differences among subdiffraction coupled plasmonic nanorods. Nano Lett. 21:5386–93
- Baffou G, Bordacchini I, Baldi A, Quidant R. 2020. Simple experimental procedures to distinguish photothermal from hot-carrier processes in plasmonics. *Light Sci. Appl.* 9:108
- Seemala B, Therrien AJ, Lou M, Li K, Finzel JP, et al. 2019. Plasmon-mediated catalytic O₂ dissociation on Ag nanostructures: hot electrons or near fields? ACS Energy Lett. 4:1803–9
- Zhang X, Li X, Reish ME, Zhang D, Su NQ, et al. 2018. Plasmon-enhanced catalysis: distinguishing thermal and nonthermal effects. Nano Lett. 18:1714–23
- 112. Zhan C, Chen X-J, Yi J, Li J-F, Wu D-Y, Tian Z-Q. 2018. From plasmon-enhanced molecular spectroscopy to plasmon-mediated chemical reactions. *Nat. Rev. Chem.* 2:216–30
- Christopher P, Moskovits M. 2017. Hot charge carrier transmission from plasmonic nanostructures. *Annu. Rev. Phys. Chem.* 68:379–98
- Wu K, Chen J, McBride JR, Lian T. 2015. Efficient hot-electron transfer by a plasmon-induced interfacial charge-transfer transition. Science 349:632–35
- Keller EL, Frontiera RR. 2018. Ultrafast nanoscale Raman thermometry proves heating is not a primary mechanism for plasmon-driven photocatalysis. ACS Nano 12:5848–55
- Brandt NC, Keller EL, Frontiera RR. 2016. Ultrafast surface-enhanced Raman probing of the role of hot electrons in plasmon-driven chemistry. J. Phys. Chem. Lett. 7:3179–85
- Brooks JL, Warkentin CL, Saha D, Keller EL, Frontiera RR. 2018. Toward a mechanistic understanding of plasmon-mediated photocatalysis. *Nanophotonics* 7:1697–724
- Martirez JMP, Bao JL, Carter EA. 2021. First-principles insights into plasmon-induced catalysis. Annu. Rev. Phys. Chem. 72:99–119
- Lee SA, Link S. 2021. Chemical interface damping of surface plasmon resonances. Acc. Chem. Res. 54:1950–60
- Lombardi A, Schmidt MK, Weller L, Deacon WM, Benz F, et al. 2018. Pulsed molecular optomechanics in plasmonic nanocavities: from nonlinear vibrational instabilities to bond-breaking. *Phys. Rev. X* 8:011016
- Flick J, Rivera N, Narang P. 2018. Strong light-matter coupling in quantum chemistry and quantum photonics. Nanophotonics 7:1479–501
- Roelli P, Galland C, Piro N, Kippenberg TJ. 2016. Molecular cavity optomechanics as a theory of plasmon-enhanced Raman scattering. Nat. Nanotechnol. 11:164–69
- Schmidt MK, Esteban R, González-Tudela A, Giedke G, Aizpurua J. 2016. Quantum mechanical description of Raman scattering from molecules in plasmonic cavities. ACS Nano 10:6291–98
- Brawley ZT, Storm SD, Contreras Mora DA, Pelton M, Sheldon M. 2021. Angle-independent plasmonic substrates for multi-mode vibrational strong coupling with molecular thin films. J. Chem. Phys. 154:104305
- Wan W, Yang X, Gao J. 2016. Strong coupling between mid-infrared localized plasmons and phonons. Opt. Express 24:12367–74
- Menghrajani KS, Nash GR, Barnes WL. 2019. Vibrational strong coupling with surface plasmons and the presence of surface plasmon stop bands. ACS Photon. 6:2110–16
- Menghrajani KS, Chen M, Dholakia K, Barnes WL. 2022. Probing vibrational strong coupling of molecules with wavelength-modulated Raman spectroscopy. Adv. Opt. Mater. 10:2102065
- Jin X, Cerea A, Messina GC, Rovere A, Piccoli R, et al. 2018. Reshaping the phonon energy landscape
 of nanocrystals inside a terahertz plasmonic nanocavity. Nat. Commun. 9:763
- Hertzog M, Munkhbat B, Baranov D, Shegai T, Börjesson K. 2021. Enhancing vibrational light–matter coupling strength beyond the molecular concentration limit using plasmonic arrays. *Nano Lett.* 21:1320– 26. Erratum. 2021. *Nano Lett.* 21:5548
- Menghrajani KS, Fernandez HA, Nash GR, Barnes WL. 2019. Hybridization of multiple vibrational modes via strong coupling using confined light fields. Adv. Opt. Mater. 7:1900403

- 131. Li TE, Cui B, Subotnik JE, Nitzan A. 2022. Molecular polaritonics: chemical dynamics under strong light–matter coupling. *Annu. Rev. Phys. Chem.* 73:43–71
- Dunkelberger AD, Simpkins BS, Vurgaftman I, Owrutsky JC. 2022. Vibration-cavity polariton chemistry and dynamics. Annu. Rev. Phys. Chem. 73:429–51
- Mecklenburg M, Hubbard WA, White ER, Dhall R, Cronin SB, et al. 2015. Nanoscale temperature mapping in operating microelectronic devices. Science 347:629–32
- 134. Idrobo JC, Lupini AR, Feng T, Unocic RR, Walden FS, et al. 2018. Temperature measurement by a nanoscale electron probe using energy gain and loss spectroscopy. *Phys. Rev. Lett.* 120:095901
- Valeur B, Berberan-Santos MN. 2012. Molecular Fluorescence: Principles and Applications. Weinheim, Ger.: Wiley-VCH. 2nd ed.
- Coppens ZJ, Li W, Walker DG, Valentine JG. 2013. Probing and controlling photothermal heat generation in plasmonic nanostructures. Nano Lett. 13:1023–28
- 137. Jaque D, Vetrone F. 2012. Luminescence nanothermometry. Nanoscale 4:4301–26
- Zhou J, del Rosal B, Jaque D, Uchiyama S, Jin D. 2020. Advances and challenges for fluorescence nanothermometry. Nat. Methods 17:967–80
- Adhikari S, Spaeth P, Kar A, Baaske MD, Khatua S, Orrit M. 2020. Photothermal microscopy: imaging the optical absorption of single nanoparticles and single molecules. ACS Nano 14:16414

 –45
- 140. Szymanski HA. 1967. Raman Spectroscopy: Theory and Practice. New York: Plenum Press
- 141. Maher RC, Cohen LF, Gallop JC, Le Ru EC, Etchegoin PG. 2006. Temperature-dependent anti-Stokes/Stokes ratios under surface-enhanced Raman scattering conditions. J. Phys. Chem. B 110:6797–803
- Inagaki M, Isogai T, Motobayashi K, Lin K-Q, Ren B, Ikeda K. 2020. Electronic and vibrational surfaceenhanced Raman scattering: from atomically defined Au(111) and (100) to roughened Au. Chem. Sci. 11:9807–17
- Inagaki M, Motobayashi K, Ikeda K. 2020. In situ surface-enhanced electronic and vibrational Raman scattering spectroscopy at metal/molecule interfaces. *Nanoscale* 12:22988–94
- 144. Lin K-Q, Yi J, Zhong J-H, Hu S, Liu B-J, et al. 2017. Plasmonic photoluminescence for recovering native chemical information from surface-enhanced Raman scattering. Nat. Commun. 8:14891
- Barnett SM, Harris N, Baumberg JJ. 2014. Molecules in the mirror: how SERS backgrounds arise from the quantum method of images. Phys. Chem. Chem. Phys. 16:6544

 –49
- Mahajan S, Cole RM, Speed JD, Pelfrey SH, Russell AE, et al. 2010. Understanding the surfaceenhanced Raman spectroscopy "background." J. Phys. Chem. C 114:7242–50
- 147. Fast A, Potma EO. 2019. Coherent Raman scattering with plasmonic antennas. Nanophotonics 8:991–1021
- 148. Jones S, Andrén D, Karpinski P, Käll M. 2018. Photothermal heating of plasmonic nanoantennas: influence on trapped particle dynamics and colloid distribution. ACS Photon. 5:2878–87
- Jollans T, Caldarola M, Sivan Y, Orrit M. 2020. Effective electron temperature measurement using time-resolved anti-Stokes photoluminescence. J. Phys. Chem. A 124:6968–76
- Fang Y, Seong N-H, Dlott DD. 2008. Measurement of the distribution of site enhancements in surfaceenhanced Raman scattering. Science 321:388–92



Contents

Remembering the Work of Phillip L. Geissler: A Coda to His
Scientific Trajectory Gregory R. Bowman, Stephen J. Cox, Christoph Dellago, Kateri H. DuBay, Joel D. Eaves, Daniel A. Fletcher, Layne B. Frechette, Michael Grünwald, Katherine Klymko, JiYeon Ku, Ahmad K. Omar, Eran Rabani, David R. Reichman, Julia R. Rogers, Andreana M. Rosnik, Grant M. Rotskoff, Anna R. Schneider, Nadine Schwierz, David A. Sivak, Suriyanarayanan Vaikuntanathan, Stephen Whitelam, and Asaph Widmer-Cooper
Gas-Phase Computational Spectroscopy: The Challenge of the Molecular Bricks of Life Vincenzo Barone and Cristina Puzzarini
Magneto-Optical Properties of Noble Metal Nanostructures **Juniper Foxley and Kenneth L. Knappenberger Jr:
Ultrafast X-Ray Probes of Elementary Molecular Events Daniel Keefer, Stefano M. Cavaletto, Jérémy R. Rouxel, Marco Garavelli, Haiwang Yong, and Shaul Mukamel
Spectroscopic Studies of Clusters of Atmospheric Relevance Nicoline C. Frederiks, Annapoorani Hariharan, and Christopher J. Johnson99
Photoacid Dynamics in the Green Fluorescent Protein **Jasper J. van Thor and Paul M. Champion** 123
Photochemical Upconversion Jiale Feng, Jessica Alves, Damon M. de Clercq, and Timothy W. Schmidt
Adsorption at Nanoconfined Solid–Water Interfaces Anastasia G. Ilgen, Kevin Leung, Louise J. Criscenti, and Jeffery A. Greathouse 169
The Predictive Power of Exact Constraints and Appropriate Norms in Density Functional Theory Aaron D. Kaplan, Mel Levy, and John P. Perdew
Modeling Anharmonic Effects in the Vibrational Spectra of High-Frequency Modes Edwin L. Sibert III

Disorder Using Site-Specific Exciton-Coupled Dimer Probe Spectroscopy Andrew H. Marcus, Dylan Heussman, Jack Maurer, Claire S. Albrecht, Patrick Herbert, and Peter H. von Hippel	245
In Situ Measurement of Evolving Excited-State Dynamics During Deposition and Processing of Organic Films by Single-Shot Transient Absorption Zachary S. Walbrun and Cathy Y. Wong	267
Toward Ab Initio Reaction Discovery Using the Artificial Force Induced Reaction Method Satoshi Maeda, Yu Harabuchi, Hiroki Hayashi, and Tsuyoshi Mita	287
Interactive Quantum Chemistry Enabled by Machine Learning, Graphical Processing Units, and Cloud Computing Umberto Raucci, Hayley Weir, Sukolsak Sakshuwong, Stefan Seritan, Colton B. Hicks, Fabio Vannucci, Francesco Rea, and Todd J. Martínez	313
Many-Body Effects in Aqueous Systems: Synergies Between Interaction Analysis Techniques and Force Field Development Joseph P. Heindel, Kristina M. Herman, and Sotiris S. Xantheas	337
Surface-Mediated Formation of Stable Glasses Peng Luo and Zahra Fakhraai	361
3D Super-Resolution Fluorescence Imaging of Microgels Oleksii Nevskyi and Dominik Wöll	391
Photodarkening, Photobrightening, and the Role of Color Centers in Emerging Applications of Lanthanide-Based Upconverting Nanomaterials Changhwan Lee and P. James Schuck	415
Isotope Effects and the Atmosphere Julia M. Carlstad and Kristie A. Boering	439
The Optical Signatures of Stochastic Processes in Many-Body Exciton Scattering Hao Li, S.A. Shah, Ajay Ram Srimath Kandada, Carlos Silva, Andrei Piryatinski, and Eric R. Bittner	467
Ultrafast Dynamics of Photosynthetic Light Harvesting: Strategies for Acclimation Across Organisms Olivia C. Fiebig, Dvir Harris, Dihao Wang, Madeline P. Hoffmann, and Gabriela S. Schlau-Cohen	493

Mechanisms of Photothermalization in Plasmonic Nanostructures:	
Insights into the Steady State	
Shengxiang Wu and Matthew Sheldon	521
Modeling Excited States of Molecular Organic Aggregates for	
Optoelectronics	
Federico J. Hernández and Rachel Crespo-Otero	547

Errata

An online log of corrections to *Annual Review of Physical Chemistry* articles may be found at http://www.annualreviews.org/errata/physchem